Influence of Void Fraction Calculation on Fidelity of CFD-DEM Simulation of Gas-Solid Bubbling Fluidized Beds

Zhengbiao Peng and Elham Doroodchi
Priority Research Centre for Advanced Particle Processing and Transport, Discipline of Chemical Engineering,
School of Engineering, The University of Newcastle, Callaghan, NSW 2308, Australia

Caimao Luo and Behdad Moghtaderi
Discipline of Chemical Engineering, School of Engineering, The University of Newcastle, Callaghan,
NSW 2308, Australia

The correct calculation of cell void fraction is pivotal in accurate simulation of two-phase flows using a computational fluid dynamics-discrete element method (CFD-DEM) approach. Two classical approaches for void fraction calculations (i.e., particle centroid method or PCM and analytical approach) were examined, and the accuracy of these methodologies in predicting the particle-fluid flow characteristics of bubbling fluidized beds was investigated. It was found that there is a critical cell size (3.82 particle diameters) beyond which the PCM can achieve the same numerical stability and prediction accuracy as those of the analytical approach. There is also a critical cell size (1/19.3 domain size) below which meso-scale flow structures are resolved. Moreover, a lower limit of cell size (1.63 particle diameters) was identified to satisfy the assumptions of CFD-DEM governing equations. A reference map for selecting the ideal computational cell size and the suitable approach for void fraction calculation was subsequently developed. © 2014 American Institute of Chemical Engineers AIChE J, 60: 2000–2018, 2014
Keywords: CFD, fluidization, numerical solutions, particulate flows, solids processing

Introduction

Gas-solid bubbling fluidized beds are commonly encountered in chemical, pharmaceutical, minerals, and food processing industries offering a high quality contact between the solid and fluid phases. The design and operation of the bubbling fluidized beds strongly rely on accurate predictions of the gas-solid two-phase flow characteristics.[1] The computational fluid dynamics-discrete element method (CFD-DEM) has shown to be effective in capturing the majority of macroscale and microscale characteristics of the two-phase flow while providing an insight into the underlying science specifically at particle-scale.[2–4] The quality of the simulation of gas-solid bubbling fluidized beds, however, is found to be strongly dependent on the accurate account of the particles impact on the fluid flow.

In the CFD-DEM numerical approach, the presence of solid particles in the two-phase flow is taken into account through the introduction of local void fraction and fluid-solid interacting terms in governing equations.[5] The fluid-solid interacting terms are often described as a function of local void fraction, particle Reynolds number, and local particle-size distribution (if polydispersed particles are dealt with).[6–10] The local void fraction defined as the fraction of gas or liquid volume in a finite computational cell is often calculated based on the vol-

ume occupied by the solid phase (i.e., cell void fraction = 1 − solid volume fraction).

The solid volume fraction in a cell is calculated mainly by three approaches, namely the particle centroid method (PCM), the analytical approach, and the alternatively nonanalytical approach. In PCM, if a particle centroid is inside a cell, the entire body of the particle is treated to be in that cell and hence the cell void fraction is calculated based on the total volume of the particle. The analytical approach, however, uses geometrical-based methods to exactly calculate the actual volume of the particle in each cell. Alternatively, the nonanalytical approaches also accurately calculate the solid fraction in a cell by relating particles to the cell through approximate schemes rather than by the geometrical relationships between the particles and the cell as in the analytical approach.

Apparently the treatment using the entire body of a particle in PCM may lead to errors of up to 50% in the calculation of solid volume of a particle when the particle centroid is near the cell boundaries. Such large errors in particle segment volume may result in incorrect prediction of local void fraction and ultimately lead to unrealistic behavior in the model outputs if the computational cell size is not large enough. Several research groups[11–15] have attempted to improve the conventional PCM. For example, Zhao and Shan[13] developed an improved PCM to accurately calculate the solid volume in a fluid cell based on the relative location of particles to the cell. Their results exemplified the potential pitfall associated with the conventional PCM when dealing

with situations where the center of the concerned particle crosses the boundary of two neighboring cells. The improved PCMs reported in the literature were found to significantly alleviate the inaccuracy of conventional PCM in the context of those studies.

Analytical approaches have been developed to completely overcome the inaccuracy associated with PCM for calculating the cell void fraction.[16,17] The analytical approach, however, was found to be largely limited to one- and two-dimensional (1-D and 2-D) systems and for rather simple geometries with spherical particles. Wu et al.[18] developed a three-dimensional (3-D) analytical approach for typical non-structured meshes (i.e., tetrahedral, wedged, or hexahedral) and spherical particles by geometrical calculation. The implementation of the approach, however, requires all detailed information on the meshes (node, edge, face, cell, and interconnections between them).

Indeed, for complex computational domains and/or irregular-shaped particles, it is extremely difficult to implement the analytical approach to calculate cell void fraction. To circumvent this problem, alternative nonanalytical approaches have been proposed by a number of researchers, including: (1) using porous cubes to represent real particles[19,20]; (2) statistically averaging approach[21,22]; (3) subelement methods[23,24]; and (4) spherical control volume method.[25–27] The advantage of these nonanalytical approaches is the flexibility to handle complex domain geometries. However, the simplistic nature of these approaches often compromises the accuracy of the predictions.

In addition to the void fraction calculation, the accuracy of the CFD-DEM model predictions using PCM is shown to be highly dependent on the cell-to-particle size ratio, with large cell-to-particle size ratios often providing the same quality predictions as those of the analytical approach. However, it should be noted that increasing the cell size beyond a critical value could compromise the fluid flow simulation. In other words, it is essential to keep the cell size sufficiently small compared to the macroscopic characteristic length of the system, so major small-scale flow structures (i.e., meso-scale flow structures in dense gas-solid flows)[28] can be resolved and hence realistic two-phase flow features can be captured. van Wachem et al.[29] found that the length of one gas-phase cell should be in the order of 4–10 particle diameters, whereas Wang et al.[30] suggested the cell size be of the order of 2–4 particle diameters and Tsuji et al.[31] pointed out the cell size should be in the range of 3–5 particle diameters. Clearly, there is no consensus on the cell size that meets the requirements for the application of PCM and also provides a reasonable solution of the fluid flow. Moreover, according to the assumptions (i.e., local mean fluid variables) for the derived continuity and Navier–Stokes equations of the fluid-phase flow in the CFD-DEM model,[5] the cell size cannot be too small compared to the particle size. However, to the best of our knowledge, no publications so far have been found quantitatively dealing with this lower limit of cell size to satisfy the assumptions of CFD–DEM governing equations and, thus, allow for the valid application of the CFD–DEM model. A general rule or a reference map for the selection of the ideal computational cell size is of much importance for CFD–DEM simulations.

The aim of the present study was to investigate the influence of the accuracy of cell void fraction calculation on the fidelity of CFD–DEM simulations of two-phase flows in the context of gas-solid bubbling fluidized beds. To this end, the conventional PCM and the analytical approach were used for the calculation of cell void fraction. The influence of void fraction calculated by PCM on CFD-DEM simulation results was first demonstrated. Analysis of the cell size requirements for the application of PCM and the reasonable solution of fluid flow was then carried out. The lower limit of cell-to-particle size ratio to satisfy the assumptions used in deriving the CFD-DEM governing equations was also investigated. Subsequently a reference map was developed for the selection of the ideal computational cell size and the suitable approach for calculating the cell void fraction in CFD-DEM simulations. The experimental data by van Wachem et al.[29] was used as the benchmark for the comparison and validation of simulation results.

Mathematical Model

Governing equations

In a dense fluid-solid flow, a single particle is interacting with neighboring particles, surrounding fluid, and computational domain boundaries. In general, the total force acting on a particle comprises collision contact forces, fluid forces, and a gravitational force. The equations for the translational and rotational motion of particle i are

$$m_i \frac{d\mathbf{v}_i}{dt} = \mathbf{f}_{\mathrm{c},i} + \mathbf{f}_{\mathrm{f},i} + m_i \mathbf{g} \qquad (1)$$

and

$$I_i \frac{d\boldsymbol{\omega}_i}{dt} = \mathbf{T}_i \qquad (2)$$

A soft-sphere model, specifically the linear spring-dashpot model,[31–33] was used in the present study to calculate the total collision contact force $\mathbf{f}_{\mathrm{c},i}$. For brevity, the details of this model are not given here.

The total fluid force ($\mathbf{f}_{\mathrm{f},i}$) results principally from the distortion of fluid streamlines passing around the particle and the subsequent variation of local fluid stress tensor at the particle surface. In a fluid-solid flow, the total fluid force acting on particle i is expressed as

$$\mathbf{f}_{\mathrm{f},i} = [-V_i \nabla p + V_i (\nabla \cdot \boldsymbol{\tau}_\mathrm{f})] + \varepsilon \mathbf{f}_{\mathrm{d},i} \qquad (3)$$

On the right-hand side of Eq. 3, the first term can be regarded as the contribution from macroscopic variations of the fluid stress tensor, and the second term represents the contribution from the detailed variation of the point stress tensor as the fluid flows around the particle.[5]

The local averaged continuity and momentum equations of the continuum are[5]

$$\frac{\partial (\varepsilon \rho_\mathrm{g})}{\partial t} + \nabla \cdot (\varepsilon \rho_\mathrm{g} \mathbf{u}_\mathrm{g}) = 0 \qquad (4)$$

$$\frac{\partial (\varepsilon \rho_\mathrm{g} \mathbf{u}_\mathrm{g})}{\partial t} + \nabla \cdot (\varepsilon \rho_\mathrm{g} \mathbf{u}_\mathrm{g} \mathbf{u}_\mathrm{g}) = -\nabla p + \nabla \cdot \boldsymbol{\tau}_\mathrm{f} + \mathbf{f}_{\mathrm{sg}} + \varepsilon \rho_\mathrm{g} \mathbf{g} \qquad (5)$$

where $\mathbf{f}_{\mathrm{sg}}$ is the local mean particle-fluid interaction force, which is calculated based on the Newton's third law by

$$\mathbf{f}_{\mathrm{sg}} = -\sum_{i=1}^{N_\mathrm{p}} \mathbf{f}_{\mathrm{f},i} / \Delta V_\mathrm{c} \qquad (6)$$

Considering the small dynamic viscosity of gas [at the order of 10^{-5} kg/(m·s) for air] and the significant density

difference between the solid particle and the gas, the term of viscous stress tensor gradient in the equation of fluid forces (i.e., Eq. 3) is ignored in the present study. The validation of this approximation is given in Appendix A. Similar treatment to the viscous stress tensor gradient has been reported in the literature.[31,34] Accordingly, Eq. 3 reads

$$\mathbf{f}_{f,i} = -V_i \nabla p + \varepsilon \mathbf{f}_{d,i} \qquad (3a)$$

Substituting Eqs. 3a and 6 into Eq. 5, the momentum equation of the fluid flow becomes

$$\frac{\partial (\varepsilon \rho_g \mathbf{u}_g)}{\partial t} + \nabla \cdot (\varepsilon \rho_g \mathbf{u}_g \mathbf{u}_g) = -\varepsilon \nabla p + \nabla \cdot (\tau_f) + \mathbf{f}'_{sg} + \varepsilon \rho_g \mathbf{g} \qquad (5a)$$

where $\mathbf{f}'_{sg} = -\sigma \varepsilon \mathbf{f}_{d,i}$ and $\sigma = N_p / \Delta V_c \cdot \mathbf{f}_{d,i}$ is the fluid drag force and calculated by

$$\mathbf{f}_{d,i} = \frac{V_i}{(1-\varepsilon)} \beta (\mathbf{u}_g - \mathbf{v}_i) \qquad (7)$$

where β is the interphase momentum exchanging coefficient and calculated by the Gidaspow draw law through the following expressions

$$\beta = \begin{cases} \dfrac{150(1-\varepsilon)^2 \mu_g}{d_p^2 \varepsilon} + \dfrac{1.75(1-\varepsilon)\rho_g |\mathbf{u}_g - \mathbf{v}_i|}{d_p} & (\varepsilon \leq 0.8) \\ 0.75 C_d \dfrac{\rho_g \varepsilon (1-\varepsilon) |\mathbf{u}_g - \mathbf{v}_i|}{d_p} \varepsilon^{-2.65} & (\varepsilon > 0.8) \end{cases} \qquad (8)$$

where C_d is the drag coefficient and givens as

$$C_d = \begin{cases} 0.44 & (\mathrm{Re}_p \leq 1000) \\ \dfrac{24}{\mathrm{Re}_p} \left(1 + 0.15 \mathrm{Re}_p^{0.687}\right) & (\mathrm{Re}_p > 1000) \end{cases} \qquad (9)$$

Re_p is the particle Reynolds number based on the superficial slip velocity between the particle and the fluid and calculated by

$$\mathrm{Re}_p = \frac{\rho_g d_p \varepsilon |\mathbf{u}_g - \mathbf{v}_i|}{\mu_g} \qquad (10)$$

The CFD-DEM model implemented in the present study is the pressure gradient force (PGF) model extensively described in the literature.[5,22,35] It should be noted that, however, to correctly implement the two-way coupling calculation, the fluid forces acting on a particle were calculated as the point forces at the (central) position of a particle to consider the distribution of particles in a cell.[29,36,37] The forces returned from particles to fluid (i.e., interphase momentum exchange terms, $\mathbf{f}'_{sg}$ in Eq. 5a) were calculated as the sum of fluid forces acting on each particle multiplied by the particle (segment) volume fraction in the cell.[18,26] More details with respect to the implementation of the interphase coupling are given in the following subsections.

Mapping scheme from Eulerian variables to point values

When calculating fluid-particle interaction forces, point values of fluid velocity and cell void fraction at the particle position are required. For convenience, the point value of a variable at the particle position is denoted as ϕ_p. Conventionally, an area (in 2-D) or volume (in 3-D) weighted aver-

aging technique, also called bilinear interpolation as described by Hoomans et al.[38] has been used to obtain these point values from surrounding computational nodal values, expressed by

$$\phi_p = \frac{1}{\Delta V_c} \sum_{i=1}^{N_n} V_i \phi_i \qquad (11)$$

where V_i is the bilinear volume function of the weighting factor for ϕ_i. However, this nodal averaging technique may lead to excessive smoothing of the heterogeneity of the local variable variation within the cell.[12] Moreover, when using unstructured meshes, the above averaging technique becomes difficult to implement due to the unavailability of proper bilinear weighting function.

In the present study, we calculated the point values of Eulerian variables based on their spatial gradient distribution by[39]

$$\phi_p = \phi_c + (\mathbf{x}_p - \mathbf{x}_c) \cdot \frac{\displaystyle\sum_{i=1}^{N_f} (\phi_{f,i} \mathbf{A}_{f,i})}{\Delta V_c} \qquad (12)$$

where ϕ_c is the variable value stored at the cell center and ϕ_f is the face value interpolated by adjacent cells following a certain numerical scheme (e.g., central-differenced, second-order upwind, and third-order Monotone Upstream-centered Scheme for Conservation Laws [MUSCL]). Equation 12 gives first-order accuracy of point values in a computational cell through a Taylor series expansion.

Calculation of cell void fraction

To study the influence of the accuracy of cell void fraction calculation on CFD-DEM simulation results, the conventional PCM and the analytical approach were used to calculate the cell void fraction.
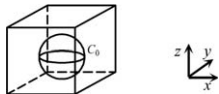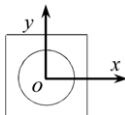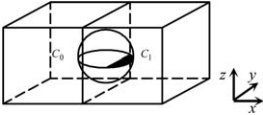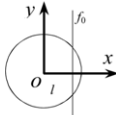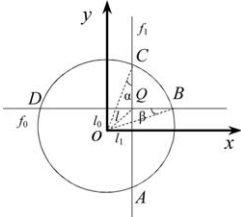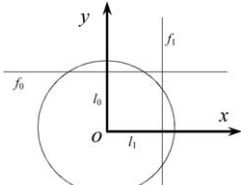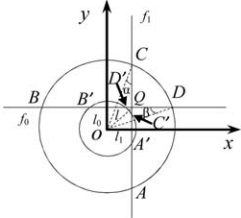
In the analytical approach, four scenarios may possibly be encountered when a particle is spanning over a number of structured cells, depending on the relative position of the particle to the vertical and horizontal cell faces. Here, O represents the particle centroid and cell c0 denotes the cell that contains the particle centroid. A new coordinate system is established with point O as the origin point (see Table 1). The analytical expressions for each scenario of particle-cell geometrical relation are given in Table 1. The overlap between wall and particles is negligible given the large spring stiffness used in the simulations. However, the overlap has also been calculated and considered in the present analytical approach, although this consideration would not make significant difference in the prediction results.

Robust implementation of particle-fluid interactions

The dynamic effects of the presence of discrete particles in a fluid flow are commonly taken into account by the terms involving cell void fraction and particle-fluid interaction forces. These two terms are often treated explicitly in the numerical solutions.[31,33,35] However, the explicit treatment of particle-fluid forces may induce convergence difficulty in the solution of a dense gas-solid flow.[40] In the present study, we calculated the particle-fluid forces semi-implicitly by treating the particle velocity ($\mathbf{v}_i$) implicitly, as detailed below.

As the nonlinear momentum exchanging coefficient β is a function of $\mathbf{u}_g$ and $\mathbf{v}_i$, we first explicitly linearize β using $\mathbf{u}_g$

Table 1. Analytical Approach for the Calculation of Cell Void Fraction

Scenario		Perspective View	Top View	Particle Fractional Volume
A				$V_{p,c0}=V_p$
B				$V_{p,c1}=\pi l^2\left(r_p-l/3\right) \quad V_{p,c0}=V_p-V_{p,c0}$
C	I			$V_{p,c2}=V_{E-BQC-F}=2\int_{0}^{h_E}A_{BQC}(z)dz$ $V_{p,c1}=V_{E-CQD-F}=\pi(r_p-l_0)^2\left(r_p-\frac{r_p-l_0}{3}\right)-V_{p,c2}$ $V_{p,c3}=V_{E-AQB-F}=\pi(r_p-l_1)^2\left(r_p-\frac{r_p-l_1}{3}\right)-V_{p,c2}$ $V_{p,c0}=V_{E-DQA-F}=V_p-V_{p,c1}-V_{p,c2}-V_{p,c3}$ $A_{BQC}(z)=\frac{1}{2}\left(\frac{\pi}{2}-\arcsin\left(\frac{l_0}{\sqrt{r_p^2-z^2}}\right)-\arcsin\left(\frac{l_1}{\sqrt{r_p^2-z^2}}\right)\right)\left(r_p^2-z^2\right)$ $-\frac{1}{2}l_0\sqrt{r_p^2-z^2-l_0^2}-\frac{1}{2}l_1\sqrt{r_p^2-z^2-l_1^2}+l_0l_1$
	II			$V_{p,c1}=\pi(r_p-l_0)^2\left(r_p-\frac{r_p-l_0}{3}\right)$ $V_{p,c2}=0$ $V_{p,c3}=\pi(r_p-l_1)^2\left(r_p-\frac{r_p-l_1}{3}\right)$ $V_{p,c0}=V_p-V_{p,c1}-V_{p,c3}$
D	I			$V_{p,c6}=V_{E-BQC}=\int_{h_Q}^{h_E}A_{BQC}(z)dz$ $V_{p,c2}=V_{BQC-F}=V_{E-BQC-F}-V_{E-BQC}=V_{E-BQC-F}-V_{p,c6}$ $V_{p,c5}=V_{E-DQC}=\int_{h_Q}^{r_p}(A_{BCDB}(z)-A_{BQC}(z))dz V_{p,c1}$ $=V_{DQC-F}=V_{E-DQC-F}-V_{E-DQC}=V_{E-DQC-F}-V_{p,c5}$ $V_{p,c7}=V_{E-AQB}=\int_{h_Q}^{r_p}(A_{ABCA}(z)-A_{BQC}(z))dz$ $V_{p,c3}=V_{AQB-F}=V_{E-AQB-F}-V_{E-AQB}=V_{E-AQB-F}-V_{p,c7}$ $V_{p,c4}=V_{E-AQD}=\pi(r_p-h_Q)^2\left(r_p-\frac{r_p-h_Q}{3}\right)-V_{p,c5}$ $-V_{p,c6}-V_{p,c7}$ $V_{p,c0}=V_{AQD-F}=V_{E-AQD-F}$ $-V_{E-AQD}=V_{E-AQD-F}-V_{p,c4}$
	II			$V_{p,c5}=\int_{h_Q}^{r_p}A_{DCD}(z)dz$ $V_{p,c1}=\pi(r_p-l_0)^2\left(r_p-\frac{r_p-l_0}{3}\right)-V_{p,c5}$ $V_{p,c7}=\int_{h_Q}^{r_p}A_{ABA}(z)dz$ $V_{p,c3}=\pi(r_p-l_1)^2\left(r_p-\frac{r_p-l_1}{3}\right)-V_{p,c7}$ $V_{p,c4}=\pi(r_p-h_Q)^2\left(r_p-\frac{r_p-h_Q}{3}\right)-V_{p,c5}-V_{p,c7}$ $V_{p,c0}=V_p-V_{p,c1}-V_{p,c5}-V_{p,c3}-V_{p,c7}-V_{p,c4}$
D	III			$V_{p,c5}=\int_{h_Q}^{r_p}A_{B'D'B'}(z)dz$ $V_{p,c7}=\int_{h_Q}^{r_p}A_{A'C'A'}(z)dz$ $V_{p,c2}=2\int_{0}^{\sqrt{r_p^2-l^2}}A_{BQC}(z)dz$ $V_{p,c1}=\pi(r_p-l_0)^2\left(r_p-\frac{r_p-l_0}{3}\right)-V_{p,c5}-V_{p,c2}$ $V_{p,c3}=\pi(r_p-l_1)^2\left(r_p-\frac{r_p-l_1}{3}\right)-V_{p,c7}-V_{p,c2}$ $V_{p,c3}=\pi(r_p-h_Q)^2\left(r_p-\frac{r_p-h_Q}{3}\right)-V_{p,c5}-V_{p,c7}$ $V_{p,c0}=V_p-V_{p,c1}-V_{p,c2}-V_{p,c3}-V_{p,c4}-V_{p,c5}-V_{p,c7}$

h: vertical distance from a point to the local coordinate origin O; z: vertical position of a x-y plane in the local coordinate; f_0, f_1: vertical cell faces that cut the particle.

and $\mathbf{v}_i$ at the previous time step according to the drag law of Gidaspow.[41] Other terms such as pressure gradient and interphase slip velocities are evaluated implicitly. The linearization of β leads to a system of linear equations. If only the fluid drag force and PGF are considered as fluid forces, then the particle velocity can, thus, be calculated by

$$m_i\left(\mathbf{v}_i^{n+1}-\mathbf{v}_i^n\right)=\left(-V_i\nabla p^{n+1}+\frac{V_i\beta_i^n}{1-\varepsilon^{n+1}}\left(\mathbf{u}_g^{n+1}-\mathbf{v}_i^{n+1}\right)\right)\Delta t_s \tag{13}$$

Based on the value of $\mathbf{v}_i^{n+1}$ and abiding by the Newton's third law, the fluid-particle interaction forces are obtained. The interphase momentum exchange terms are subsequently calculated by summing up the fluid-particle interaction forces on each particle in the cell, weighted by the particle fractional volume as detailed above. Through the synchronized calculations of particle velocity and gas flow velocity, the two-way coupling gets numerically enhanced and significantly increase the solution convergence time.[39,40] The calculation of fluid field normally converges within 15–20 iteration steps for the majority of simulations conducted in this study, while the explicit scheme requires around 32.9% more iteration steps to converge and correspondently expends 16.1% extra CPU time to complete the simulation of the same gas-solid flow time. In summary, the overall algorithm for the code implementation of the CFD-DEM simulation of a fluid-particle flow follows the routine described in Figure 1.

Numerical Strategy and Methodologies

The semi-implicit method for pressure-linked equation (SIMPLE) algorithm was used to solve the pressure-velocity coupling equations of the fluid flow, namely the continuity and momentum conservation equations (i.e., Eqs. 4 and 5a). The quadratic upwind interpolation of convective kinematics (QUICK) scheme was used for the spatial discretization of the convection term. The diffusion term was discretized by a central-differenced scheme that always is of second-order accuracy. The Green-Gauss Node-Based method was used to calculate the variable gradients for constructing values of a scalar at cell faces and also for computing secondary diffusion terms and velocity derivatives. A uniform gas flow was introduced from the bottom inlet of the domain. The impermeable nonslip condition was applied at the solid wall boundaries and the pressure outlet boundary condition was applied for the outflow.

The validation of simulation results was carried out using the experimental data of van Wachem et al.[29] For the purpose of validations, the geometry of the simulated domain (i.e., pseudo-2-D) and particle (polystyrene) properties were kept exactly the same as those in the experimental work of van Wachem et al.[29] The detailed conditions and parameters used in the simulations are listed in Table 2. The values of restitution coefficient and the friction coefficient are taken from literature.[12,29] Sensitivity of simulation results to the value of particle spring stiffness has been evaluated prior to commencing the numerical study. The result showed that the local and bulk gas-solid flow characteristics were almost independent of the value of spring stiffness over the values ranging between 10^3 and 10^4 N/m. For the sake of accuracy, a value of 10^4 N/m for the spring stiffness has been chosen for all computational cases in this study, corresponding to a
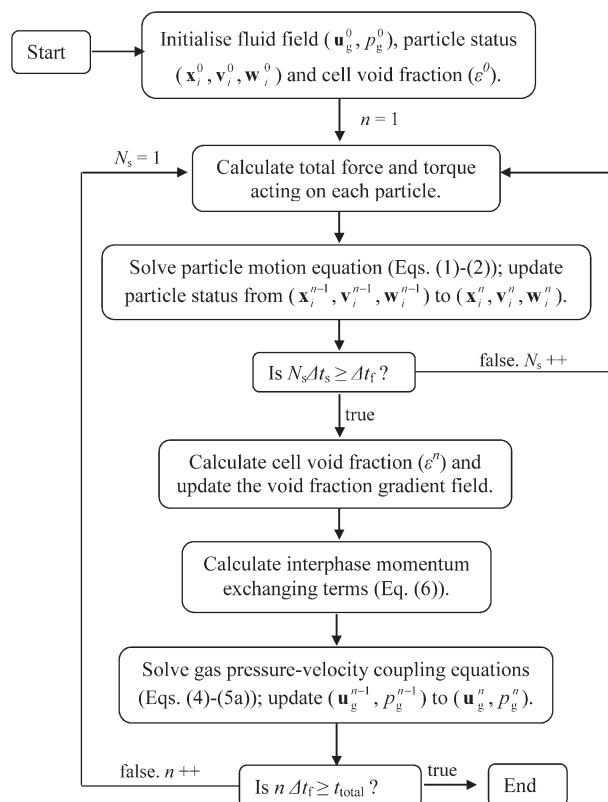
Figure 1. Flow chart of the overall algorithm for the code implementation of the CFD-DEM two-way coupling simulation of a fluid-particle flow.

solid time step of 5×10^{-6} s and a maximum particle normal overlap of 0.0013 r_p (averaging over 10 s simulation) under the inlet velocity of $U_{sf} = 0.9$ m/s. The total torque in Eq. 2 was generated only by the tangential contact force, and the contribution by the rolling resistance[42,43] was ignored. Details on the examination of the rolling resistance torque are given in Appendix B. In each time step, the globally scaled residual of 10^{-4} has been set as the convergence criteria for solving gas-phase equations (i.e., Eqs. 4 and 5a). The starting point of the solid phase was consistent in all simulations with particles randomly packed in the bed. After starting the gas flow, a time period of 5 s was set to allow the gas-solid flow to reach the statistical steady state. The data in the statistical steady state (5–10 s) were used for analysis and discussion. Multithread parallel computation (OpenMP) based on the shared memory was used to improve the computational efficiency. For a typical parallel simulation with 4000 meshes on two computational nodes (clock speed 2.66 GHz, Smart Cache 12 M, and QPI speed 6.4GT/s), it expends around 58.5 h to complete the simulation of 10 s gas-solid flow.

It is worth mentioning that as PCM is simply based on the centroids of a particle and the computational cell, no further calculations (e.g., particle cutting by cell faces, particle segment volume, and intersection between cell edges and particle segments as in the analytical approach) are required. Therefore, the PCM code execution is much simpler. However, due to the inaccurate calculation of cell void fraction, using PCM leads to difficulties in reaching numerical convergence and often requires more iterations in each time

Fluid Phase	
Domain size (mm^3)	$90 \times 8 \times 500$
Gas density (kg/m^3)	1.125
Gas viscosity (Pa·s)	1.8 e -5
Gas superficial velocity (m/s)	0.9, 1.3, 1.8, 2.3
Fluid time step (s)	1×10^{-4}
Solid Phase	
Particle diameter (mm)	1.545
Particle density (kg/m^3)	1150
Particle mass (kg)	0.039
Normal spring-stiffness (N/m)	10^4
Restitution coefficient ($-$)	0.9
Friction coefficient ($-$)	0.3
Solid time step (s)	5×10^{-6}

step. As a result, the CFD-DEM solver using the analytical approach showed better overall computational performance than the solver using PCM, saving around 24% simulation CPU time for typical runs in the present study.

Results and Discussion

Considering the domain geometry and the cell shape are rarely cubic in practical systems, here an effective length based on the volume has been defined to represent the domain size, S_d, and the cell size, S_c. In this study, S_d and S_c are calculated by

$$S_d = \sqrt[3]{V_d} = \sqrt[3]{l_x l_y l_z}, \quad S_c = \sqrt[3]{V_c} = \sqrt[3]{\Delta l_x \Delta l_y \Delta l_z} \quad (14)$$

The results of the simulations are presented in terms of ratios involving S_d and S_c.

### Influence of void fraction calculations by PCM on simulation results

The fluid dynamics in a gas-solid fluidized bed is typically characterized by the pressure signal characteristics of the bed.[44] In the present simulations, we monitored the time series of the local pressure. Figure 2 shows the fluctuation of the cross-section averaged pressure at a height of 5 mm above the distributor, predicted using PCM and the analytical approach to calculate the cell void fraction in a densely meshed domain with $S_c/d_p = 2.38$. It can be seen that while keeping a reasonable average value, the transient pressure fluctuates with unreasonably high amplitude with peak values reaching as high as 2491 Pa when PCM was used. The observed fluctuations are much greater than those exhibited by the analytical approach. The high amplitude fluctuations observed using PCM can be explained as follows. When the cell size is small in the order of a particle size, it is very likely for a particle to span over several cells. The particle, however, is only affiliated with the cell in which its centroid is residing. The void fraction of the other cells containing part of this particle is calculated not taking into account the volume of this particle. As a result, the void fraction of the affiliated cell could become unrealistically low, for example, 0.1423 under conditions of Figure 2. With such a low cell void fraction, the drag force term in Eq. 5a becomes unrealistically large, which in turn destabilizes the solution of fluid flow. Moreover, the earlier incorrect calculation of cell void fraction leads to temporally unsmooth void fraction variation, which also renders the solution unstable as the governing equations of the gas-solid two-phase flow include a term containing the time derivative of cell void fraction. Note that

in the simulations with PCM, a threshold value of 0.35 was set for the cell void fraction to avoid the sudden abort of the solution as a result of local extremes. However, the incorrect cell void fraction calculated by PCM renders the simulation results unrealistic and, thus, the unreasonable pressure spike was observed in the simulation. Using the analytical approach, the average value of the transient pressure over the last 5 s of the two-phase flow was found to be 509 Pa, which is in excellent agreement with the reported pressure drop of 480 Pa (i.e., 6% error) measured by van Wachem et al.[29]

Moreover, the normalized net mass flow rate was monitored as a criterion of solution convergence and a measure satisfying the mass conservation law to reflect the numerical stability of the solution. The normalized net mass flow rate is defined as the mass flow rate difference of inlet and outlet normalized by the inlet mass flow rate, expressed as

$$\Psi_m = \frac{\sum \Lambda_{f,in} + \sum \Lambda_{f,out}}{\sum \Lambda_{f,in}} \quad (15)$$

where $\Lambda_f = \rho_g \mathbf{u}_g \mathbf{A}_f \varepsilon_f$ is the mass flow rate through the cell face. Subscripts "in" and "out" denote the inlet and outlet of the computational domain. ε_f is the cell face void fraction, which is an interpolated value from the cell void fraction. Figure 3 shows the time series of the normalized net mass flow rate in the simulation using PCM and the analytical approach for $S_c/d_p = 2.38$. It can be seen that when using PCM to calculate the cell void fraction, the net mass flow rate reaches up to 30% of the inlet mass flow rate at some time instants. It simply suggests that the solution does not even satisfy the mass conservation law and implies the simulation has not or will never reach a converged solution. The inaccurate cell void fraction leads to the unrealistic solution of the fluid flow, which gives rise to the imbalanced gas flow flux across the faces of this cell. Conversely, with the analytical approach, the normalized net mass flow rate was found to be less than 0.0005%, implying the mass conservation law is strictly satisfied in the present two-way coupling solution. Note that the convergence criterion for the pressure-velocity coupling solution is based on the scaled
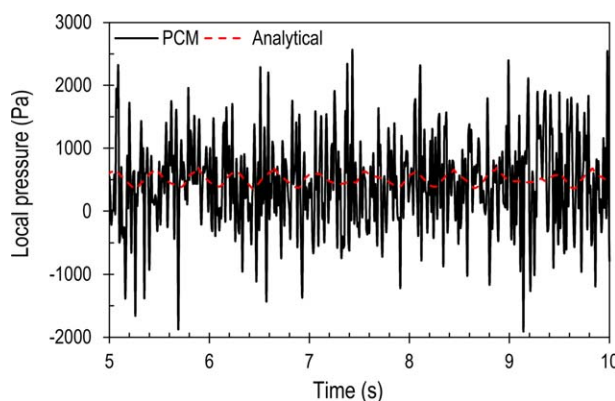
Figure 2. Local pressure fluctuation samples taken at $U_{sf} = 0.9$ m/s for $S_c/d_p = 2.38$ at 5 mm above the distributor using PCM and analytical approach for calculating the cell void fraction.

[Color figure can be viewed in the online issue, which is available at wileyonlinelibrary.com.]
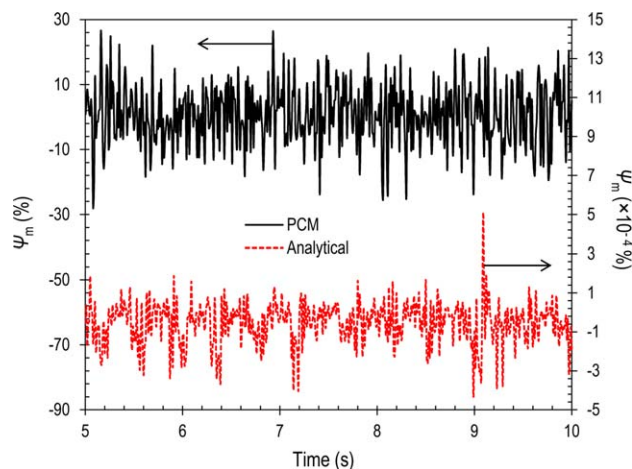
Figure 3. Time series of the normalized net mass flow rate using PCM and analytical approach for calculating the cell void fraction at $U_{sf} = 0.9$ m/s for $S_c/d_p = 2.38$.

[Color figure can be viewed in the online issue, which is available at wileyonlinelibrary.com.]

residuals, which were calculated every iteration by summing up the local absolute residual over all computational cells and then normalizing the sum by the largest value in the first five iterations. The convergence criterion of the normalized net mass flow rate is often met earlier than those of the scaled residuals. As a result, the obtained normalized net mass flow rate is very low (in the order of 1 e −6). Some noises are also observed due to the round off errors in the fluctuation.[37]

Critical S_c/d_p for applying PCM

Critical Value of S_c/d_p. The application of PCM for calculating cell void fraction over cell-to-particle size ratios (S_c/d_p) ranging between 1.39 and 7.41 (i.e., fine to coarse cells) was examined and its effect on CFD-DEM simulations was investigated. For the purpose of comparison, simulations using the analytical approach have also been performed with the same cell-to-particle size ratios. Two quantities were used to verify the validity of PCM in the CFD-DEM simulations:

1. The maximum local pressure obtained using PCM normalized by that using the analytical approach, that is, $\chi = p_{max,\ PCM}/p_{max,\ analytical}$. According to Eq. 5a, the incorrect calculation of cell void fraction by PCM affects the final flowing field solution and the unreasonable pressure spike at one location was observed in our numerical results, which leads to $\chi \gg 1.0$. If a simulation using PCM is stable, the predicted values of local pressure should be comparable to those using the analytical approach, that is, $\chi \approx 1$.

2. The maximum value of normalized net mass flow rate (defined in Eq. 15), denoted by $\psi_{m,\ max}$. If the solid fraction was calculated incorrectly by PCM, the unreasonable solution of the fluid flow field gives rise to high local fluid flow fluxes across cell faces, which lead to an unrealistically large $\psi_{m,\ max}$. Conversely, if the simulation using PCM is stable, $\psi_{m,\ max}$ should be negligibly small, satisfying the mass conservation law.

The data over the last 5 s of the total flow time is used for the statistical analysis. Figure 4a shows the dependence

of χ and $\psi_{m,\ max}$ on S_c/d_p (1.39–7.41) at $U_{sf} = 0.9$ m/s. As S_c/d_p increases (i.e., the cells become coarse), both χ and $\psi_{m,\ max}$ decrease indicating the diminishing impact of the inaccurate cell void fraction calculated by PCM. This is because as the cell size increases, the fraction of the particle volume that is incorrectly being treated becomes negligible compared to the cell volume. A significant drop is observed in the values of both χ and $\psi_{m,\ max}$ when S_c/d_p varies from 3.79 to 4.77. For easy identification, the results in this transition region (i.e., $S_c/d_p = 3.79$–4.77) were shown separately in Figure 4b, in which more ratios of S_c/d_p with a small incremental step were used. It can be seen that as S_c/d_p increases beyond 3.82, χ varies around 1.0 and $\psi_{m,\ max}$ falls approaching values around 0.001%. These results indicate that PCM can provide stable simulations with similar results to those using the analytical approach for $S_c/d_p \geq 3.82$. Hence $S_c/d_p = 3.82$ can be regarded as the critical value, greater than which PCM can be used with confidence in CFD-DEM simulations.

Discussion on the Critical S_c/d_p. The above analyses were performed at $U_{sf} = 0.9$ m/s for particles with a minimum fluidization velocity (U_{mf}) of 0.74 m/s. The average bed voidage under these conditions given by the revised
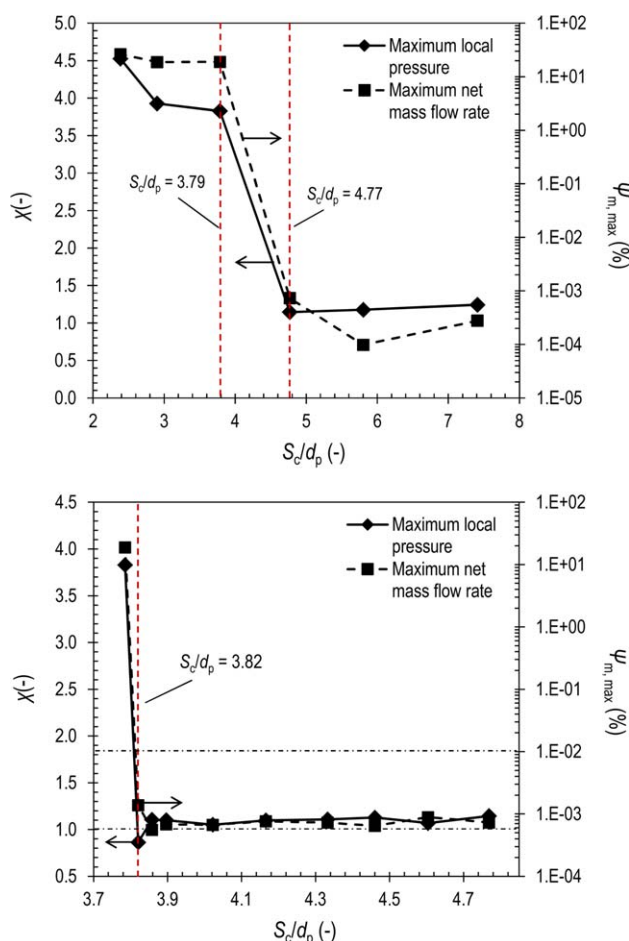
Figure 4. Normalized maximum local pressure (45 mm above the distributor) and normalized net mass flow rate as a function of the cell-to-particle size ratio at $U_{sf} = 0.9$ m/s using PCM: (a) $S_c/d_p = 1.39$–7.41; (b) $S_c/d_p = 3.79$–4.77.

[Color figure can be viewed in the online issue, which is available at wileyonlinelibrary.com.]
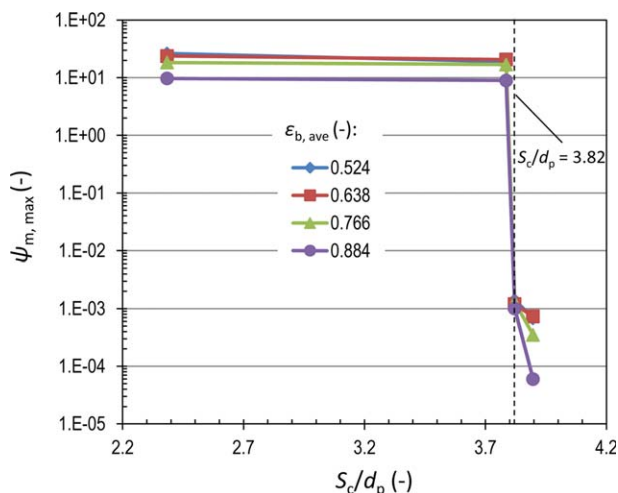
Figure 5. Maximum value of normalized net mas flow rate as a function of cell-to-particle size ratio for different flow regimes.

[Color figure can be viewed in the online issue, which is available at wileyonlinelibrary.com.]

Ergun equation[45] is 0.524, which represents a relatively dense system. Here we examined the validity of the critical S_c/d_p for systems with different bed voidages, corresponding to different flow regimes (i.e., dense or dilute flow). Specifically, the superficial gas velocity was altered to change the flow regime with the average bed voidage $\varepsilon_{b, ave}$ varying between 0.524 and 0.88 (i.e., from dense to dilute). For a specific average bed voidage (or flow regime), cell-to-particle size ratios around the critical value (i.e., 2.38, 3.79, 3.82, and 3.9) have been used in the simulations.

Figure 5 shows the variation of the maximum value of the normalized net mass flow rate as a function of cell-to-particle size ratio for different flow regimes ($\varepsilon_{b,ave} = 0.524$–0.884). It can be seen that for $S_c/d_p < 3.82$, $\psi_{m, max}$ is over 8.95% in all flow regimes. It means that the mass conservation law is not satisfied to a reasonable accuracy in the simulation due to the incorrect void fraction calculation in computational cells. However, $\psi_{m, max}$ consistently decreases to a value below 0.001% in all flow regimes as S_c/d_p increases and exceeds the value of 3.82. Therefore, it can be concluded that the critical $S_c/d_p = 3.82$ is independent of flow regimes.

Moreover, as discussed above, the numerical instability of a CFD-DEM simulation using PCM results primarily from the small cell-to-particle-size ratio used for the simulation. As the critical S_c/d_p obtained above (i.e., Figure 4) was based on the analysis of numerical stability of the simulation, the critical S_c/d_p is, thus, mainly dependent on the cell-to-particle-size ratio used in the simulation. Other simulation parameters, that is, particle size and particle properties (e.g., density, spring stiffness, and restitution coefficient) may generate different simulation outputs, but have no impact on the accuracy of solid fraction calculation and hence the numerical stability of the simulation. Therefore the critical value of S_c/d_p (i.e., 3.82) is also independent of other simulation parameters (i.e., particle size and particle properties).

Critical S_c for the solution of the two-phase flow

When the cell void fraction is accurately calculated using the analytical approach, the CFD-DEM simulation is numeri-

cally stable and the quality of simulation results is determined merely by the computational cell size.

According to the definition of local mean variables for the flowing field by Anderson and Jackson,[5] the cell size should be small enough compared with the scale of "macroscopic" variations from point to point in the system and large enough compared with the particle spacing. In other words, on one hand, the computational cells need to be sufficiently fine compared to the macroscopic characteristic length of the system to resolve major small-scale structures of the fluid flow, especially flow structures formed on subgrid scales.[28,30,46] To this end, S_d was used to represent the macroscopic characteristic length of the system. Subsequently, the ratio of S_d/S_c describes the extent of the small magnitude of the computational cell size S_c when compared to the macroscopic characteristic length S_d. S_d/S_c also quantifies the domain resolution, that is, how fine the computational cells actually are for solving the fluid flow in the domain. On the other hand, the computational cell size cannot be too small compared to the particle size, otherwise assumptions used to derive the governing equations of the CFD-DEM model (i.e., local mean fluid variables), are not satisfied.[5] Here, the cell-to-particle size ratio (i.e., S_c/d_p) is used to describe how many particles may possibly be contained in a cell.

The influence of domain resolution (i.e., S_d/S_c) on the simulation results and the lower limit of S_c/d_p to satisfy the assumptions of CFD-DEM governing equations have been investigated, as detailed below.

Influence of Domain Resolution (S_d/S_c) on the Solution of the Two-Phase Flow. In the simulations, only the computational cell size was altered. All other simulation parameters including domain size S_d and particle size d_p remained unchanged. Therefore, S_d/S_c and S_c/d_p were both changing when S_c was altered. However, the reverse of dimensionless cell size S_d/S_c was used in the discussion of this subsection to describe the domain resolution.

Figure 6 shows the snapshots of particles location over time fluidized at $U_{sf} = 0.9$ m/s. The gas-solid flow in a gas bubbling fluidized bed exhibits periodic features owing to the evolution of bubbles, that is, from formation at the bottom to eruption at the top. Therefore, snapshots of particle location in a time period of 0.36 s of the gas-solid flow showing a complete period of a bubble evolution in the statistical steady state (i.e., after 5 s) was compared against those measured in experiments by van Wachem et al.[29] The top time series of snapshots (Figure 6a) presents the experimental data of van Wachem et al.,[29] and Figures 6b–f are the simulation results using S_d/S_c between 7.9 and 22.9. As S_d/S_c is changed, three distinct gas-solid flow patterns are observed. At $S_d/S_c \geq 19.3$ (Figures 6b,c), the simulation reproduces the gas-solid bubbling flow behavior captured in the experiments.[29] Specifically, the bubble size, shape, and evolution including bubble formation, growth, coalescence, eruption, and burst as well as the overall particle fluidization characteristics such as bed expansion and bed oscillation frequency are visually the same. Conversely, the simulated gas-solid bubbling behavior is found to be significantly different from the experimental observations as S_d/S_c is reduced to 17.4 and 12.2 (i.e., Figures 6d,e). In particular, the bubble sizes are much smaller than those observed in experiments. The bubble rising rate increases and as a result the bubble has a shorter duration of evolution from formation to eruption. The bed expansion height also becomes lower than that
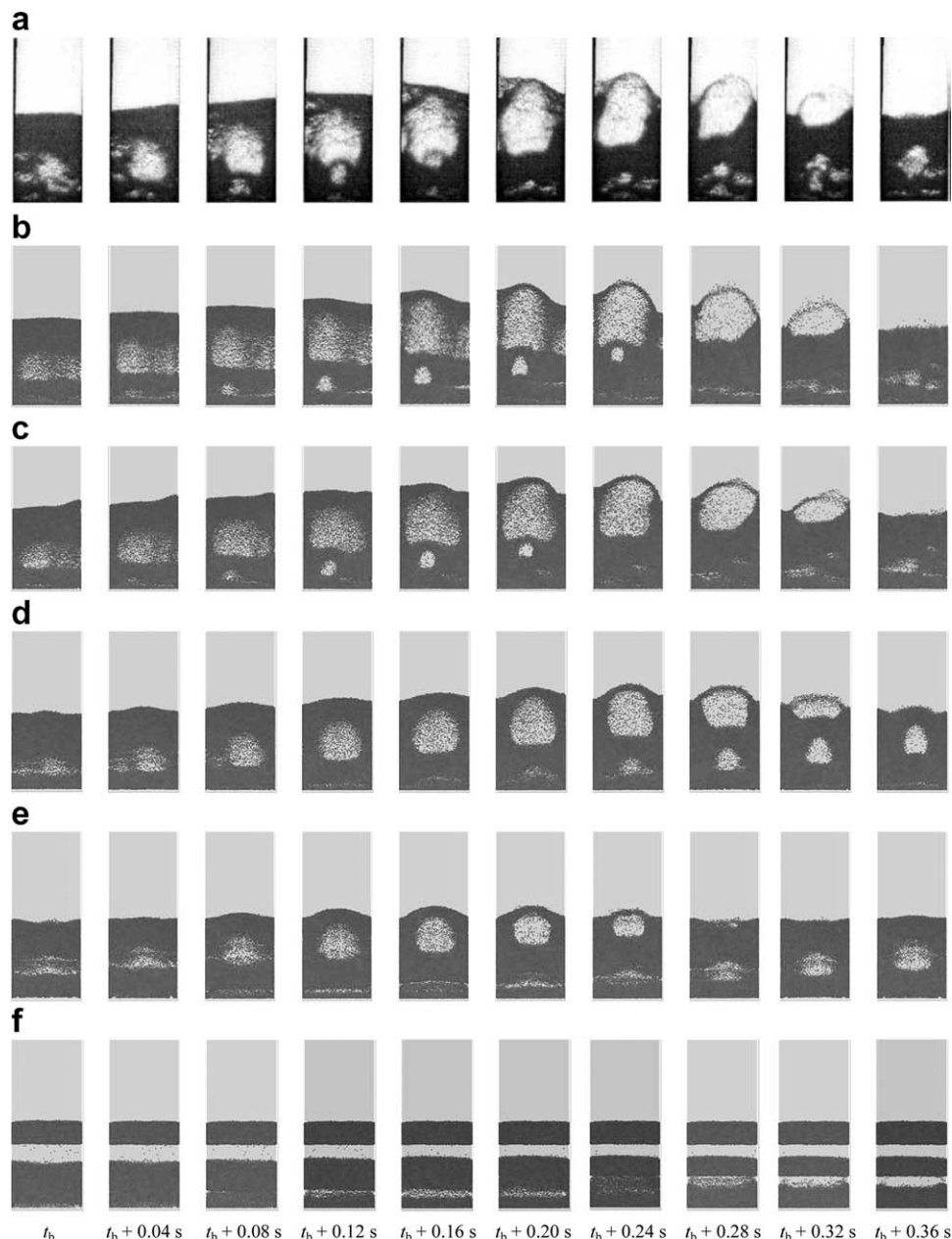
Figure 6. Snapshots of particles location over time at $U_{sf} = 0.9$ m/s: (a) experiment; (b) simulation with $S_d/S_c = 22.9$; (c) simulation with $S_d/S_c = 19.3$; (d) simulation with $S_d/S_c = 17.4$; (e) simulation with $S_d/S_c = 12.2$; (f) simulation with $S_d/S_c = 7.9$; t_b is the beginning time of the series of snapshots showing the complete period of a bubble evolution in the statistical steady state of the simulation.

in experiments and has a faster oscillation frequency. In Figure 6e with $S_d/S_c = 12.2$, the bubble shape are nearly symmetric and the bubbles are rising along the centerline of the bed. Interestingly, when S_d/S_c decreases further to 7.9 (i.e., Figure 6f), the unexpected "slugging" fluidization regime is observed at the early stage of the simulation, followed by the formation of stratified layers of particles. The above unexpected behaviors in Figures 6d–f suggest that the solution of the two-phase flow is incorrect when using a poor domain resolution (i.e., $S_d/S_c < 19.3$).

Figure 7 shows vorticity contours on the *xz* plane at *y/2* for S_d/S_c of 7.9, 12.2, 17.4, 19.3, and 22.9 for snapshots of particle location shown at $t = t_b + 0.24$ s in Figure 6. It can be seen that as S_d/S_c increases and hence smaller cell sizes are used, the resolution of fluid flow structures becomes

greater with more small eddies generated in the fluidized bed being captured. In contrast, these small vortices do not exist at $S_d/S_c = 7.9$ (Figure 7a). That is because the important meso-scale structures of the fluid flow remain unresolved using large sized cells. These small eddies originating from the interactions between the gas flow and particles in turn are the driving mechanism for the heterogeneous motion of discrete particles. As S_d/S_c increases from 12.2 to 17.4 (i.e., Figures 7b–c), the solution of the fluid flow significantly improves with more small vortices being observed in the dense-phase region. The fluid flow field, however, appears to be symmetric, which is rather unrealistic since a bubbling fluidized bed features heterogeneous flow characteristics. The results suggest that for S_d/S_c of 12.2–17.4 the cells are not yet sufficiently fine to fully resolve the major small-scale
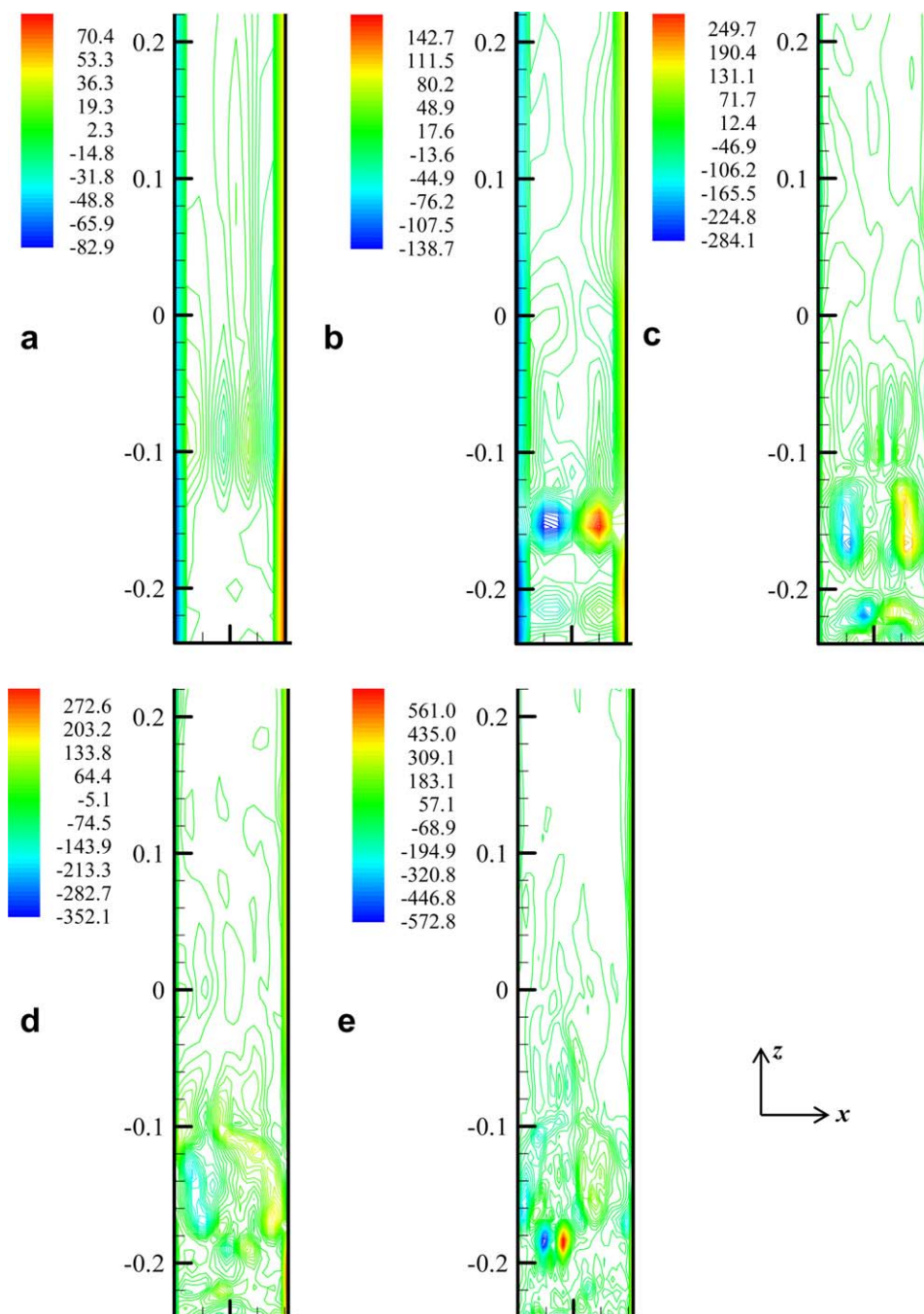
Figure 7. Vorticity contours on the *xz* plane at *y*/2 at U_{sf} = 0.9 m/s and *t* = *t*$_b$+0.24s (in Figure 6) for simulations with S_d to S_c ratios of: (a) 7.9; (b) 12.2; (c) 17.4; (d) 19.3; (e) 22.9.

[Color figure can be viewed in the online issue, which is available at wileyonlinelibrary.com.]

flow structures. The typical heterogeneous features of the gas flow are revealed as S_d/S_c becomes equal or greater than 19.3, as shown in Figures 7d–e.

The influence of S_d/S_c on the gas-solid two-phase flow characteristics was also quantitatively examined by analyzing the local pressure signals. Figure 8 demonstrates the comparison of the fluctuation of local relative pressure (45 mm above the distributor) obtained experimentally (Figure 8a)[29] with the simulation results for S_d/S_c ranging between 6.2 and 26.2 (Figures 8b–i). Generally three patterns of pressure fluctuation can be distinguished as S_d/S_c varies between 6.2 and 26.2. At $S_d/S_c \leq 7.9$ (i.e., Figure 8i), the local relative pres-

sure remained unchanged after the initial response of 1 s or so to the gas flow. This behavior corresponds with the observed stratified particle layers shown in Figure 6f. For S_d/S_c ranging from 9.7 to 15.9 (Figures 8f–h), the local pressure is fluctuating with an almost constant frequency and amplitude. The fluctuating frequency is found to be relatively high while the amplitude is low in comparison to the experimental data. These trends are indicative of faster bubbling rising rates and the formation of smaller sized bubbles.[29,44] The symmetrically shaped bubbles (Figure 6e) and the symmetric fluid field at S_d/S_c = 12.2 (Figure 7b) is consistent with the above ordered pressure fluctuation. Beyond S_d/S_c = 19.3
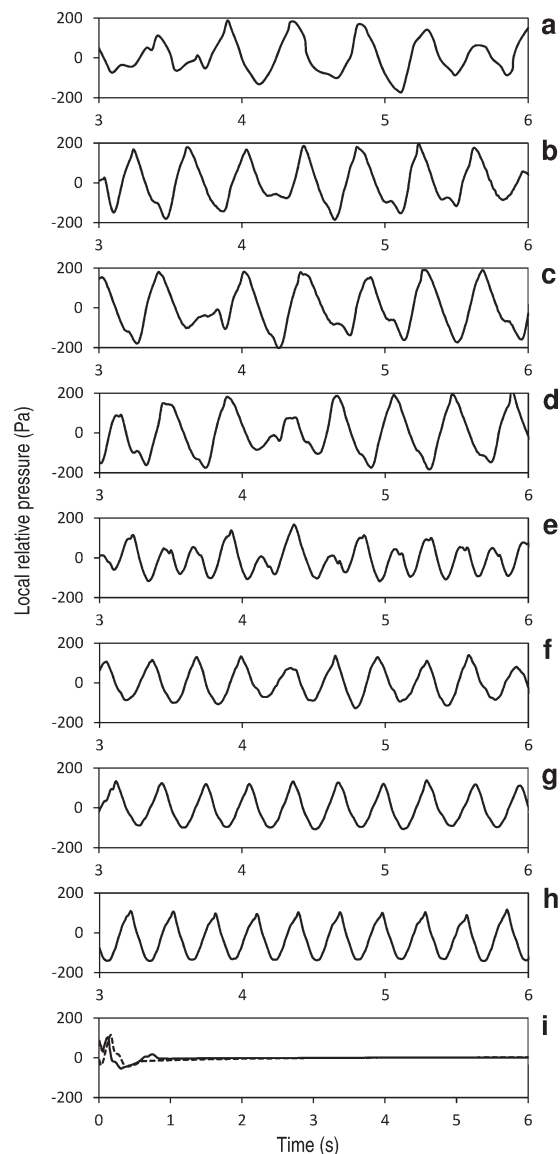
Figure 8. Local relative pressure fluctuation taken at 45 mm above the distributor at $U_{sf} = 0.9$ m/s for (a) experiment; (b) simulation with $S_d/S_c = 26.2$; (c) simulation with $S_d/S_c = 22.9$; (d) simulation with $S_d/S_c = 19.3$; (e) simulation with $S_d/S_c = 17.4$; (f) simulation with $S_d/S_c = 15.9$; (g) simulation with $S_d/S_c = 12.2$; (h) simulation with $S_d/S_c = 9.7$; (i) simulation with solid line representing $S_d/S_c = 7.9$ and dash line representing $S_d/S_c = 6.2$.

(Figures 8b–d), the pressure fluctuation in terms of frequency and amplitude shows an excellent agreement with the data obtained experimentally (Figure 8a). The above results suggest that $S_d/S_c \geq 19.3$ can be considered as a critical condition that needs to be met to satisfy the requirements of domain resolution for the fluid flow solution in the CFD-DEM simulation of a bubbling fluidized bed.

The use of a discretization scheme with a higher order of accuracy was also examined to determine if it can improve the accuracy of the solution of fluid flow and hence compensate the inaccuracy caused using a large cell size. In the present study, the third-order MUSCL scheme for the discretization of convection term of governing equations has been

adopted in the simulation with relatively coarse computational cells ($S_d/S_c = 15.87$). Table 3 shows the influence of the discretization scheme on the simulation outputs in terms of average maximum granular temperature (Θ_{max}), time series fluctuations of local bed voidage ($\varepsilon_{0.045}$), and local pressure ($p_{0.045}$) at 45 mm above the distributor, and the total pressure drop (Δp) of the fluidized bed (different from the reported pressure drop by van Wachem et al.[29] that was measured at 5 mm above the distributor). It can be observed that essentially identical results have been obtained between the third-order MUSCL scheme and the second-order QUICK scheme, indicating that the value of S_d/S_c is independent of discretization schemes for convective terms in the momentum governing equations.

Lower Limit of S_c/d_p *for CFD-DEM Simulations..* To examine the influence of S_c/d_p on simulation results using the analytical approach, simulations with fine meshes have been performed with S_c/d_p ranging between 1.29 and 1.76. The dimensionless cell size S_c/d_p was used for the discussion of this subsection to investigate the lower limit of cell-to-particle size ratio for valid CFD-DEM simulations.

The snapshots of particles location over time is shown in Figure 9 at $U_{sf} = 0.9$ m/s. The top time series of snapshots (Figure 9a) presents the experimental data of van Wachem et al.,[29] and Figures 9b–e are the simulation results using S_c/d_p between 1.39 and 1.76. Remarkably, for $S_c/d_p \geq 1.63$ (i.e., Figures 9b and c), the solid flow pattern, bubble characteristics, and fluidization behavior (as described above) predicted by the model agree excellently with those observed in experiments. However, for $S_c/d_p < 1.63$ (i.e., Figures 9d and e), clear differences exist between the experimental and the simulated bed behaviors. Specifically, the bubble sizes are much smaller and the bubble shape becomes rather irregular. The bubble has a shorter duration of evolution and consequently the bed expansion height is lower than that in experiments with a faster oscillation frequency. Moreover, the solid distribution appears more heterogeneous and more small sized bubbles are observed across the bed.

Figure 10 compares the pressure fluctuation of local relative pressure (45 mm above the distributor) predicted using different cell-to-particle size ratios against the experimental data. Figure 10a is the experimental data measured by van Wachem et al.,[29] and Figures 10b–f are the simulation results for $S_c/d_p = 1.29$–1.76. It can be seen that for $S_c/d_p \geq 1.63$ (i.e., Figures 10b and c), the predicted pressure fluctuations agree well with that measured in experiments in terms of the amplitude and frequency of the fluctuation. However, as S_c/d_p decreases below 1.63 (i.e., Figure 10d–f), the predicted pressure fluctuations apparently deviate from the experimental data with higher frequency and smaller amplitude. As the cell void fraction is accurately calculated by the analytical approach, the inaccurate prediction results obtained for $S_c/d_p < 1.63$ can be attributed to the too few solid particles present in a cell when S_c/d_p is too small. In such cases, the assumptions that were used to derive the CFD-DEM governing equations (i.e., local mean fluid variables) are no longer satisfied.[5] As a result, the uncharacteristic behavior of the gas-solid bubbling flow was obtained. The above results simply suggest that $S_c/d_p = 1.63$ can be regarded as the minimum cell-to-particle size ratio when using the CFD-DEM model for simulations. It should be also noted that the critical point $S_c/d_p = 1.63$ is applicable only when the analytical approach is used in the simulation.

Table 3. Influence of Discretization Schemes on the Simulation Results at $U_{sf} = 0.9$ m/s for $S_d/S_c = 15.87$

Discretization Scheme	Θ_{max} (m²/s²)	$\varepsilon_{0.045}$ (−)			$P_{0.045}$ (Pa)			
		Mean (−)	SD (−)	Freq. (Hz)	Mean (Pa)	SD (−)	Freq. (Hz)	ΔP (Pa)
QUCIK	0.0994	0.5693	0.1059	3.13	282.9833	72.6199	3.13	544.4603
MUSCL	0.0997	0.5668	0.1040	3.13	282.6946	69.7953	3.13	542.1363

Freq.: the dominant frequency by FFT analysis.

Reference map for selecting cell size and void fraction calculation methodology

While it is established that the selection of CFD-DEM computational cell size for simulation of a two-phase flow is largely governed by the system parameters, no consensus exists on the selection criteria. In this study, we have shown that there are several criteria, which must be met to satisfy the requirements for the application of PCM for calculating cell void fraction and for the reasonable solution of the two-phase flow. These criteria are (1) $S_c/d_p \geq 3.82$ for the valid application of PCM; (2) $S_d/S_c \geq 19.3$ to meet the requirements of domain resolution for the fluid flow solution; and (3) $S_c/d_p \geq 1.63$ to satisfy the assumptions of CFD-DEM governing equations. Taking into account these findings, we propose a reference map for the selection of computational cell size for CFD-DEM simulations based on the relationship
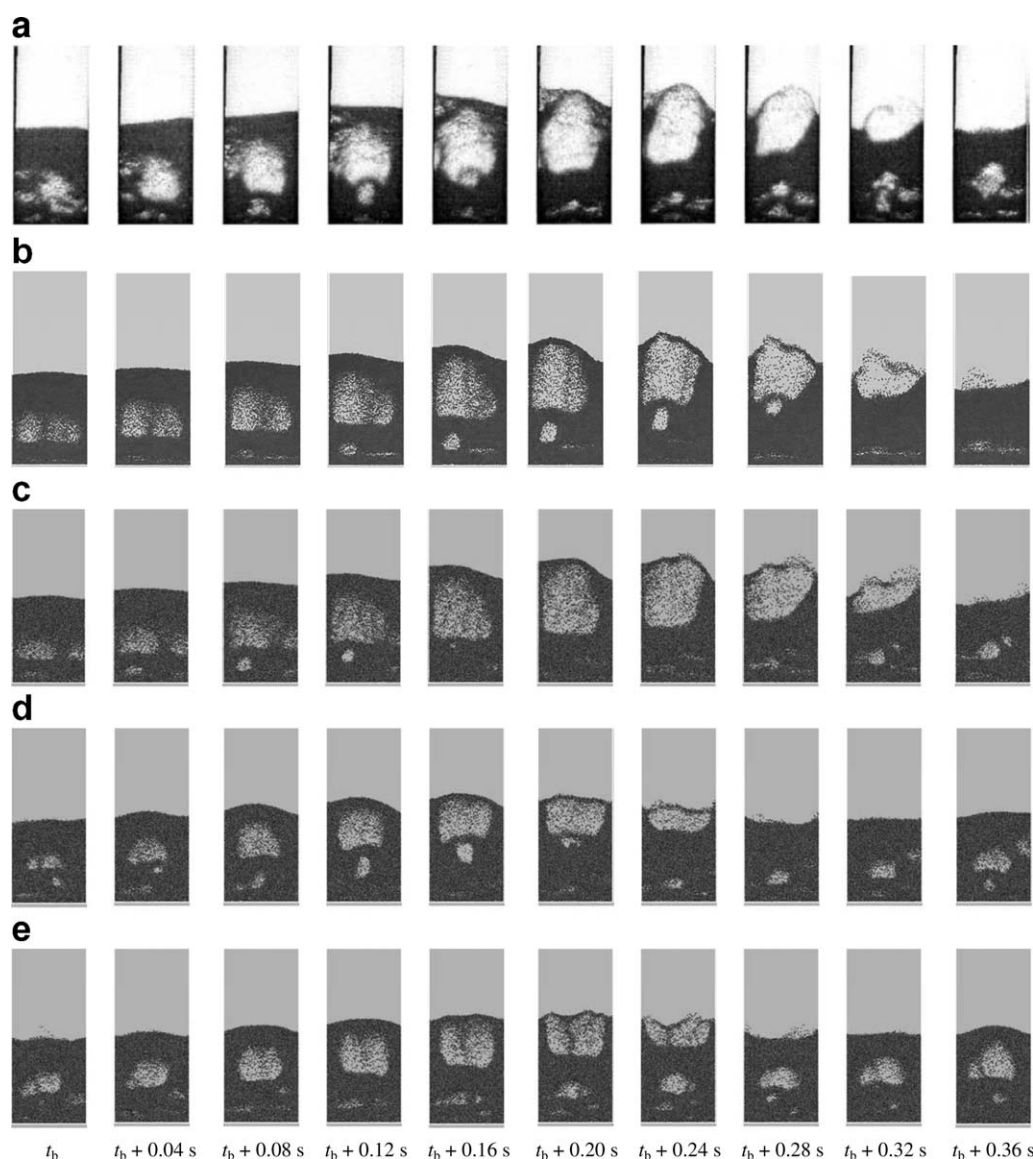
Figure 9. Snapshots of particles location over time at $U_{sf} = 0.9$ m/s: (a) experiment; (b) simulation with $S_c/d_p = 1.76$; (c) simulation with $S_c/d_p = 1.63$; (d) simulation with $S_c/d_p = 1.48$; (e) simulation with $S_c/d_p = 1.39$; t_b is the beginning time of the series of snapshots showing the complete period of a bubble evolution in the statistical steady state of the simulation.
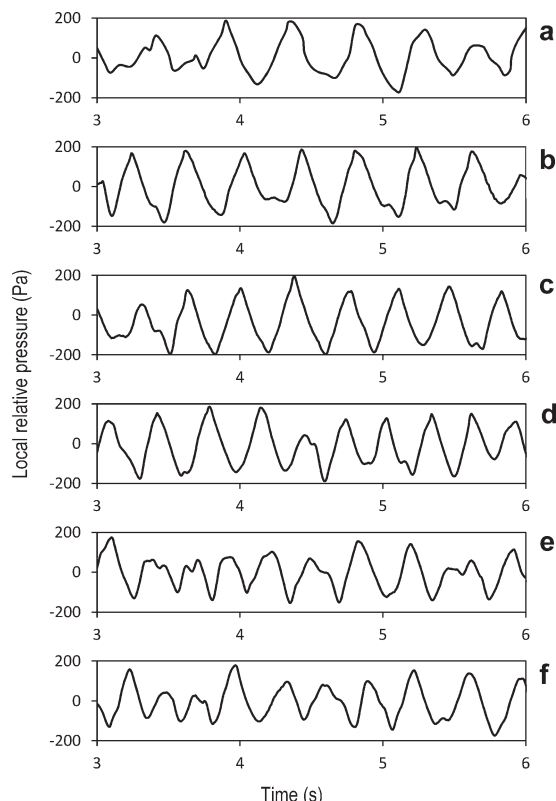
Figure 10. Local relative pressure fluctuation taken at 45 mm above the distributor at $U_{sf} = 0.9$ m/s for (a) experiment; (b) simulation with $S_c/d_p = 1.76$; (c) simulation with $S_c/d_p = 1.63$; (d) simulation with $S_c/d_p = 1.48$; (e) simulation with $S_c/d_p = 1.39$; (f) simulation with $S_c/d_p = 1.29$.

between the domain-to-cell size ratio (S_d/S_c) and the cell-to-particle size ratio (S_c/d_p). Let us consider

$$y = S_d/S_c \qquad (16)$$

and

$$x = S_c/d_p \qquad (17)$$

Dividing the numerator and denominator of Eq. 16 by particle diameter and substituting Eq. 17 in Eq. 16, the above relationship can be expressed as

$$y = \alpha \frac{1}{x} \qquad (18)$$

where $\alpha = S_d/d_p$. Equation 18 gives the function representing the family of curves for the selection of computational cell size. These curves are bounded by the limit conditions of $S_c/d_p \geq 1.63$ and $S_d/S_c \geq 19.3$. Figure 11 shows the reference map, in which lines for alpha (α) values of 40, 93, 180, 300, 450, and 650 are plotted. The white-bounded area with the plotted curves specifies the range of ideal computational cell size for a CFD-DEM simulation; accordingly the gray areas mark the regions of cell size, for which the results of a CFD-DEM simulation become questionable if not incorrect. In the region of solid lines ($S_c/d_p \geq 3.82$), either PCM or the analytical approach can be applied for calculating the cell void fraction; in the region of dash lines ($1.63 \leq S_c/d_p < 3.82$) only the analytical approach can be applied. For example, for a given domain and particle size and hence

$\alpha = S_d/d_p$, a series of cell sizes can be obtained by selecting different points on the alpha (α) curve. Depending on the position of the point on the map, a corresponding methodology can be selected for each point based on the following criteria

$$\text{Methodology}_{\text{void\_fraction}}$$
$$= \begin{cases} \text{Analytical } 1.63 \leq S_c/d_p < 3.82, S_d/S_c \geq 19.3 \\ \text{Analytical or PCM } S_c/d_p \geq 3.82, S_d/S_c \geq 19.3 \end{cases} \qquad (19)$$

To further support the validity of the proposed criteria for the selection of computational cell size and void fraction calculation methodology, the predictions of the map were compared with the literature data, as shown in Figure 12. The literature data collected for the validation are summarized in Table 4. Total of 35 articles with 47 study cases of two-phase flow simulations of fluidized beds are reported in this table. The data were reduced from the original domain and cell dimensions given in the literature. Equation 14 was used for the calculation of the effective size, namely S_d and S_c, in 3-D cases. For 2-D or pseudo-2-D cases, an area-based effective size was obtained. It should be noted that the pseudo-2-D case adopted here merely refers to those with a cell number of one along the depth direction, to fully consider the influence of cell size variation along all directions on a CFD-DEM simulation. In a few cases with binary mixtures, the larger particle size was used for the calculation as d_p. As Figure 12 shows, the majority (80.9%) of the data
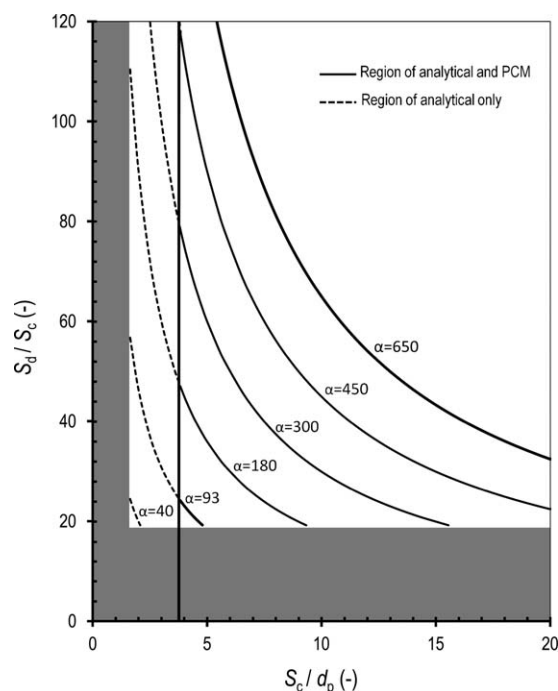
Figure 11. Reference map for selecting ideal computational cell size and the suitable approach for calculating the cell void fraction.

The white-bounded area with the plotted curves specifies the ranges of ideal computational cell size; the grey areas mark the regions of inappropriate cell sizes for CFD-DEM simulations. In the region of solid lines ($S_c/d_p \geq 3.82$), either PCM or the analytical approach can be applied for calculating the cell void fraction; in the region of dash lines ($1.63 \leq S_c/d_p < 3.82$) only the analytical approach can be applied.
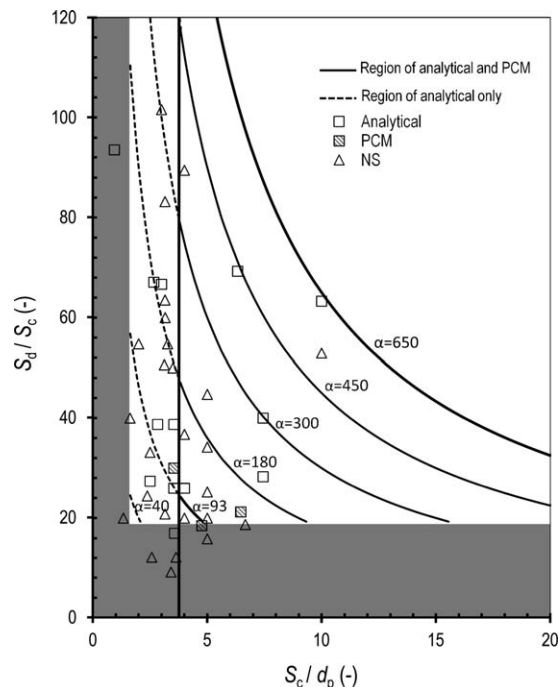
Figure 12. Validation of the reference map with data in the literature, in total 35 CFD-DEM work with 47 study cases including 2D and 3D, gas-solid and liquid-solid systems.

points fall within the range specified for an ideal cell size (i.e., the white region), indicating that the map can provide an effective guideline for selection of cell size for simulation of two-phase flows in bubbly fluidized beds.

However, a number of factors have to be considered when using the reference map in CFD-DEM simulations.

1. Discrete data points were examined to determine the critical values, as discussed above. Therefore, the critical values of $(S_c/d_p)_{PCM} = 3.82$, $(S_d/S_c)_{DR} = 19.3$, and $(S_c/d_p)_{CFD-DEM} = 1.63$ are not exact values. Error bars of 0.47, 4.77, and 4.57% (calculated by halving the interval between the critical point and the adjacent point) are expected for the critical values of $(S_c/d_p)_{PCM}$, $(S_d/S_c)_{DR}$, and $(S_c/d_p)_{CFD-DEM}$, respectively. As a result, we have $(S_c/d_p)_{PCM} = 3.82 \pm 0.02$, $(S_d/S_c)_{DR} = 19.3 \pm 0.92$, and $(S_c/d_p)_{CFD-DEM} = 1.63 \pm 0.07$.

2. This reference map was developed based on numerical experiments of gas-solid bubbling fluidized beds and serves as a reference for the selection of computational cell size and void fraction calculation methodology for a CFD-DEM simulation. Care must be taken when applied to systems with significantly different characteristics since its application to other two-phase flow systems are yet to be verified.

3. As can be observed in Table 4 and Figure 12, the reference map is applicable for both 2-D and 3-D cases and also the liquid-solid systems.

Other parameters, for example, the domain width l_x, have also been examined as the characteristic length. However, poor agreements were obtained between the reference map and the literature (i.e., Table 4) due to the different domain geometries and/or cell shapes used in those studies. For example, only 25.5% of the cited studies followed the reference map when l_x was used as the characteristic length.

Therefore, the volume-base-length S_d was adopted above as the macroscopic characteristic length to derive the reference map.

To address whether or not the reference map is problem dependent, the nondimensional analysis based on the macroscopic characteristic length of the system (i.e., S_d) has been performed. The dimensionless continuity and momentum equations of the gas flow were derived and given as below

$$\frac{\partial(\varepsilon'\rho'_g)}{\partial t'} + \nabla' \cdot (\varepsilon'\rho'_g \mathbf{u}'_g) = 0 \qquad (20)$$

$$\frac{\partial(\varepsilon'\rho'_g \mathbf{u}'_g)}{\partial t'} + \nabla' \cdot (\varepsilon'\rho'_g \mathbf{u}'_g \mathbf{u}'_g) = -\frac{p_0}{\rho_{g0}u_{g0}^2}\varepsilon'\nabla'p' + \frac{1}{Re}\varepsilon_0\nabla'$$
$$\cdot \tau'_f + \frac{1}{\varepsilon_0}\mathbf{f}'_{sg}(Re, \varepsilon) + \frac{S_d|\mathbf{g}_0|}{u_{g0}^2}\varepsilon'\rho'_g\mathbf{g}'$$

$$(21)$$

where

$$\nabla' = \frac{\partial}{\partial x'}\mathbf{i} + \frac{\partial}{\partial y'}\mathbf{j} + \frac{\partial}{\partial z'}\mathbf{k}, x' = \frac{x}{S_d}, y' = \frac{y}{S_d}, z' = \frac{z}{S_d},$$

$$\varepsilon' = \frac{\varepsilon}{\varepsilon_0}, t' = \frac{t}{S_d/u_{g0}}, \rho'_g = \frac{\rho_g}{\rho_{g0}}, \mathbf{u}'_g = \frac{\mathbf{u}_g}{u_{g0}}, p' = \frac{p}{p_0},$$

$$\tau'_f = \frac{\tau_f}{\mu u_{g0}/S_d^2}, \mathbf{f}'_{sg}(Re, \varepsilon) = \frac{\mathbf{f}_{sg}(Re, \varepsilon)}{\rho_{g0}u_{g0}^2/S_d}, \text{ and } \mathbf{g}' = \frac{\mathbf{g}}{\mathbf{g}_0}$$

where S_d is the macroscopic characteristic length; ε_0 is the bed voidage of the packed bed of the particles; ρ_{g0} is the air density; u_{g0} is the inlet gas superficial velocity; p_0 is the atmospheric pressure; $\mathbf{g}_0$ is the gravity acceleration velocity of the earth ground, that is, 9.8 m/s².

Therefore, four dimensionless numbers are obtained, that is

$$\alpha' = \frac{p_0}{\rho_{g0}u_{g0}^2}, \quad \beta' = \frac{1}{Re\,\varepsilon_0}, \quad \gamma' = \frac{1}{\varepsilon_0}, \quad \text{and } \delta' = \frac{S_d|\mathbf{g}_0|}{u_{g0}^2} \quad (22)$$

Theoretically, if the above four dimensionless numbers are the same as those in the current study, the reference map can be applied to any new problem with a different S_d. For cases with different dimensionless numbers, the majority of them, as demonstrated in Table 4 and Figure 12, follow the reference map. The results indicate that the reference map is problem independent and can be applied to other problems with a different S_d.

Conclusions

In the present study, the influence of the accuracy of cell void fraction calculation on CFD-DEM simulation results has been investigated. The requirements of computational cell size for the application of PCM and the reasonable solution of the fluid flow (i.e., meso-scale flow structures being captured) have been discussed. The lower-limit of computational cell size to satisfy the assumptions of CFD-DEM governing equations has also been investigated. Based on the results, a reference map has been developed to be used as a guideline for selecting the ideal computational cell size and a suitable approach for calculating the cell void fraction.

With a cell-to-size ratio smaller than 3.82, the numerical instability occurred in the simulation using PCM with unreasonably high local pressure and the imbalanced mass

Table 4. S_c/d_p, S_d/S_c and the Approach of Void Fraction Calculation Used in the Literature

Author	Dimension	System	d_p (mm)	S_d/d_p (-)	S_d/S_c (-)	S_c/d_p (-)	VOF approach
Amritkar et al.[47]	3D	G-S	1.2	31.26	9.16	3.41	NS
	3D	G-S	4	304.78	101.59	3.00	NS
Zhuang et al.[48]	2D	G-S	1	357.77	89.44	4	NS
Yang et al.[49]	2D	G-S	1	438.18	69.28	6.32	Analytical
Liu et al.[50]	3D	G-S	2.5	44.21	12.16	3.63	NS
Li et al.[51]	3D	G-S	1.2	31.26	12.16	2.57	NS
	3D	G-S	4.04	58.11	24.42	2.38	NS
Li et al.[52]	2D	G-S	1	223.61	44.72	5	NS
	3D	G-S	1	79.37	15.87	5	NS
	3D	G-S	1	100	20	5	NS
	3D	G-S	1	125.99	25.20	5	NS
	3D	G-S	1	171.00	34.20	5	NS
Wang et al.[53]	2D	L-S	3	88.19	93.54	0.94	Analytical
Wu et al.[12]	2D	G-S	1.545	137.3	21.21	6.47	PCM
Geng and Che[54]	Pseudo2D	G-S	3	26.67	20	1.33	NS
	Pseudo2D	G-S	1	80	20	4	NS
Norouzi et al.[55]	2D	G-S	0.65	565.27	183.71	3.08	Analytical
Zhou et al.[56]	Pseudo2D	G-S	10	146.97	36.74	4	NS
Feng et al.[57]	2D	G-S	2	65	40	1.625	NS
Li et al.[58]	2D	G-S	1	158.11	50.6	3.125	NS
Mansourpour et al.[59]	Pseudo2D	G-S	1	200	66.67	3	Analytical
Wang et al.[60]	Pseudo2D	G-S	0.075	178.89	67.08	2.67	Analytical
Wu et al.[61]	2D	G-S	0.5	632.46	63.25	10	Analytical
Hou et al.[62]	2D	G-S	0.1	109.54	54.77	2	NS
Muller et al.[63]	Pseudo2D	G-S	1.2	60.55	16.97	3.57	Analytical
Malone et al.[64]	Pseudo2D	L-S	1.5	124.72	18.71	6.67	NS
Zhang et al.[65]	2D	G-S	0.1	529.15	52.92	10	NS
Tsuji et al.[66]	3D	G-S	4	65.52	20.80	3.15	NS
	3D	G-S	4	200	63.50	3.15	NS
	3D	G-S	4	262.07	83.20	3.15	NS
Di Maio and Di Renzo[67]	Pseudo2D	G-S	0.433	178.89	54.77	3.27	NS
Di Renzo and Di Maio[32]	2D	L-S	0.2	189.74	60	3.16	NS
	2D	G-S	0.07	174.96	50	3.50	NS
Sun et al.[21]	2D	G-S	4	91.86	25.98	3.54	Analytical
	2D	G-S	2.5	103.92	25.98	4	Analytical
Wu et al.[37]	2D	G-S	2.5	109.54	38.73	2.83	Analytical
Zhong et al.[68]	3D	G-S	2	88.01	18.47	4.77	PCM
Bokker et al.[69]	Pseudo2D	G-S	2.5	103.92	25.98	4	Analytical
Ye et al.[36]	2D	G-S	0.1	82.92	33.17	2.5	NS
Li and Kuipers[70]	2D	G-S	0.95	210.75	28.28	7.45	Analytical
	2D	G-S	0.95	298.04	40	7.45	Analytical
Kafui et al.[35]	2D	G-S	4	136.93	38.73	3.54	Analytical
van Wachem et al.[29]	2D	G-S	1.55	137.3	21.21	6.47	Analytical
Xu et al.[71]	2D	G-S	4	136.93	38.73	3.54	Analytical
Xu and Yu[33]	2D	G-S	4	91.86	25.98	3.54	Analytical
Hoomans et al.[38]	2D	G-S	4	68.47	27.39	2.5	Analytical
Tsuji et al.[31]	2D	G-S	4	106.07	30	3.54	PCM

G-S: gas-solid; L-S: Liquid-solid; NS: not specified.
Total 35 papers with 47 study cases have been cited.

flow. With a cell-to-particle size ratio greater than 3.82, the simulation was stable and the results were found to be comparable with those using the analytical approach.

Using the analytical approach to calculate cell void fraction, distinct results were obtained when using different domain-to-cell size ratios. Specifically, with a domain-to-cell size ratio lower than 19.3, the solution provided unrealistic gas-solid bubbling behavior in terms of gas-solid flow pattern, bubble characteristics, fluidization behavior and local pressure fluctuation. Conversely, the simulation using a domain-to-cell size ratio greater than 19.3 reproduced the gas-solid bubbling flow behavior captured in the experiments. Hence the computational cells need to be sufficiently fine with a domain-to-cell size ratio greater than 19.3 so the important small-scale structures of the fluid flow and hence the meso-scale features of the two-phase flow can be resolved.

However, the results showed that when the computational cell size was too small with a cell-to-particle size ratio less than 1.63, the uncharacteristic behavior of the gas-solid bubbling flow was obtained due to the failure to satisfy the assumptions (i.e., local mean fluid variables) for deriving the CFD-DEM governing equations.

A reference map was developed based on the above criteria of computational cell size. When the four dimensionless numbers (i.e., Eq. 22) were the same with those in current study, the reference map can be applied with confidence to any new problem with a different S_d. For cases with different dimensionless numbers, the majority of them agreed with the predictions of the reference map. The reference map can be used as a guideline for the selection of computational cell size and the approach for the calculation of cell void fraction.

Acknowledgments

Notation

Symbols

A = area, m^2
$\mathbf{A}$ = face area factor
C_d = drag coefficient
d = particle diameter, m
$\mathbf{f}_c$ = collision contact forces acting on the particle, N
$\mathbf{f}_f$ = total fluid forces acting on the particle, N
$\mathbf{f}_d$ = drag force, N
$\mathbf{f}_{sg}$ = local mean particle-fluid interaction forces, N
$\mathbf{g}$ = acceleration of gravity, m/s^2
$\underline{I}$ = particle inertia, kg/m^2
$\overline{\mathbf{I}}$ = unit tensor
l = domain dimensions, m
m = particle mass, kg
N_p = particle number inside a cell
N_n = node number around a particle
p = pressure, Pa
r = radius, m
Re_p = particle Reynolds number
S_c = equivalent cell size, m
S_d = equivalent domain size, m
$\mathbf{T}$ = torque acting on the particle, N/m
U_{sf} = gas superficial velocity, m/s
$\mathbf{u}$ = fluid velocity vector, m/s
V_c = cell volume, m^3
V_d = domain volume, m^3
V_i = volume of particle i, m^3
$\mathbf{v}$ = particle velocity vector, m/s
$\mathbf{x}$ = coordinates of a point, m

Greek letters

α = domain-to-particle size ratio
α' = dimensionless number
β = momentum exchanging coefficient
β' = dimensionless number
γ = scaling factor
γ' = dimensionless number
δ' = dimensionless number
ε = local void fraction
Δl = cell dimensions, m
Δt_s = solid time step, s
λ = gas bulk viscosity, kg/(m·s)
μ = shear viscosity, kg/(m·s)
ρ = density, kg/m^3
τ_f = viscous stress tensor
χ = normalized maximum value of local pressure
σ = local particle number density, m^{-3}
φ = fluid variables
ψ = normalized net mass flow rate
Λ = mass flow rate through cell faces, kg/s
Θ = granular temperature, m^2/s^2
$\boldsymbol{\omega}$ = particle angular velocity, rad/s

Subscripts

c = cell
d = drag
DR = domain resolution
f = face
g = gas phase
i, j = particle index
p = particle phase
r = relative
x, y, z = direction

Literature Cited

1. Curtis JS, van Wachem B. Modeling particle-laden flows: a research outlook. *AIChE J*. 2004;50:2638–2645.
2. Zhu HP, Zhou ZY, Yang RY, Yu AB. Discrete particle simulation of particulate systems: a review of major applications and findings. *Chem Eng Sci*. 2008;63:5728–5770.
3. Peng ZB, Doroodchi E, Evans G. DEM simulation of aggregation of suspended nanoparticles. *Powder Technol*. 2012;204:91–102.
4. Guo Y, Wu CY, Thornton C. Modelling gas-particle two phase flows with complex and moving boundaries using DEM-CFD with an immersed boundary method. *AIChE J*. 2013;59:1075–1087.
5. Anderson TB, Jackson R. A fluid mechanical description of fluidized beds—equations of motion. *Ind Eng Chem Fund*. 1967;6:527–539.
6. van der Hoef MA, Beetstra R, Kuipers JAM. Lattice Boltzmann simulations of low Reynolds number flow past mono- and bidisperse arrays of spheres: results for the permeability and drag force. *J Fluid Mech*. 2005;528:233–254.
7. Beetstra R, van der Hoef MA, Kuipers JAM. Drag force of intermediate Reynolds number flow past mono- and bidisperse arrays of spheres. *AIChE J*. 2007;53:489–501.
8. Sarkar S, van der Hoef MA, Kuipers JAM. Fluid–particle interaction from lattice Boltzmann simulations for flow through polydisperse random arrays of spheres. *Chem Eng Sci*. 2009;64:2683–2691.
9. Cello F, Di Renzo A, Di Maio FP. A semi-empirical model for the drag force and fluid–particle interaction in polydisperse suspensions. *Chem Eng Sci*. 2010;65:3128–3139.
10. Holloway W, Yin X, Sundaresan S. Fluid-particle drag in inertial polydisperse gas–solid suspensions. *AIChE J*. 1995;56:1995–2004.
11. Lim EWC, Wang CH, Yu AB. Discrete element simulation for pneumatic conveying of granular material. *AIChE J*. 2006;52:496–509.
12. Wu GR, Ouyang J, Yang BX, Li Q. Use of compromise-based local porosities for coarse grid DEM simulation of bubbling fluidized bed with large particles. *Adv Powder Technol*. 2012;24:68–78.
13. Zhao JD, Shan T. Coupled CFD-DEM simulation of fluid-particle interaction in geomechanics. *Powder Technol*. 2013;239:248–258.
14. Deb S, Tafti DK. A novel two-grid formulation for fluid-particle systems using the discrete element method. *Powder Technol*. 2013;246:601–616.
15. Alobaid F, Epple B. Improvement, valiation and application of CFD/DEM model to dense gas-solid flow in a fluidized bed. *Particuology*. 2013;2013:514–526.
16. Chen F, Drumm EC, Guiochon G. Coupled discrete element and finite volume solution of two classical soil mechanics problems. *Comput Geotech*. 2011;38:638–647.
17. Li J. Euler-Lagrange Simulation of Flow Structure Flormation and Evolution in Dense Gas-Solid Flows. Ph.D. Thesis, University of Twente, The Netherlands. 2003.
18. Wu CL, Zhan JM, Li YS, Lam KS, Berrouk AS. Accurate void fraction calculation for three-dimensional discrete particle model on unstructured mesh. *Chem Eng Sci*. 2009;64:1260–1266.
19. Link JM, Cuypers LA, Deen NG, Kuipers JAM. Flow regimes in a spout–fluid bed: a combined experimental and simulation study. *Chem Eng Sci*. 2005;60:3425–3442.
20. Sutkar VS, Deen NG, Mohan B, et al. Numerical investigations of a pseudo-2D spout fluidized bed with draft plates using a scaled discrete particle model. *Chem Eng Sci*. 2013;104:790–807.
21. Sun J, Battaglia F, Subramaniam S. Hybrid Two-Fluid DEM Simulation of Gas-Solid Fluidized Beds. *J Fluid Eng T ASME*. 2007;129:1394–1403.
22. Xiao H, Sun J. Algorithms in a robust hybrid CFD-DEM solver for particle-laden flows. *Commun Comput Phys*. 2011;9:297–323.
23. Gui N, Fan JR, Luo K. DEM–LES study of 3-D bubbling fluidized bed with immersed tubes. *Chem Eng Sci*. 2008;63:3654–3663.
24. Hilton JE, Mason LR, Cleary PW. Dynamics of gas-solid fluidised beds with non-spherical particle geometry. *Chem Eng Sci*. 2010;65:1584–1596.
25. Okaya K, Sadaki J, Fujita T. Calculation of packing fraction in context of discrete element method (DEM). *J Soc Powder Technol Jpn*. 2008;45:206–212.
26. Kuang SB, Chu KW, Yu AB, Zou ZS, Feng YQ. Computational investigation of horizontal slug flow in pneumatic conveying. *Ind Eng Chem Res*. 2008;47:470–480.
27. Natsui S, Nogami H, Ueda S, Kano J, Inoue R, Ariyama T. Simultaneous three-dimensional analysis of gas-solid flow in blast furnace

28. Wang JW, van der Hoef MA, Kuipers JAM. The role of scale resolution versus inter-particle cohesive forces in two-fluid modeling of bubbling fluidization of Geldart A particles. *Chem Eng Sci*. 2011;66: 4229–4240.

29. van Wachem BGM, van der Schaaf J, Schouten JC, Krishna R, van den Bleek CM. Experimental validation of Lagrangian–Eulerian simulations of fluidized beds. *Powder Technol*. 2001;116:155–165.

30. Wang JW, van der Hoef MA, Kuipers JAM. Why the two-fluid model fails to predict the bed expansion characteristics of Geldart A particles in gas-fluidized beds: a tentative answer. *Chem Eng Sci*. 2009;64:622–625.

31. Tsuji Y, Kawaguchi T, Tanaka T. Discrete particle simulation of two-dimensional fluidized bed. *Powder Technol*. 1993;77:79–87.

32. Di Renzo A, Di Maio FP. Homogeneous and bubbling fluidization regimes in DEM–CFD simulations: hydrodynamic stability of gas and liquid fluidized beds. *Chem Eng Sci*. 2007;62:116–130.

33. Xu BH, Yu AB. Numerical simulation of the gas-solid flow in a fluidized bed by combining discrete particle method with computational fluid dynamics. *Chem Eng Sci*. 1997;52:2785–2809.

34. Lu HL, Zhao YH, Ding JM, Gidaspow D, Li W. Investigation of mixing/segregation of mixture particles in gas–solid fluidized beds. *Chem Eng Sci*. 2007;62:301–317.

35. Kafui KD, Thornton C, Adams MJ. Discrete particle-continuum $uid modelling of gas–solid fluidised beds. *Chem Eng Sci*. 2002;57:2395–2410.

36. Ye M, van der Hoef MA, Kuipers JAM. A numerical study of fluidization behavior of Geldart A particles using a discrete particle model. *Powder Technol*. 2004;139:129–139.

37. Wu CL, Zhan JM, Li YS, Lam KS. Dense particulate flowmodel on unstructured mesh. *Chem Eng Sci*. 2006;61:5726–5741.

38. Hoomans BPB, Kuipers JAM, Briels WJ, van Swaaij WPM. Discrete particle simulation of bubble and slug formation in a two-dimensional gas-fluidised bed: a hard-sphere approach. *Chem Eng Sci*. 1996;51:99–118.

39. Wu CL, Berrouk AS, Nandakumar K. Three-dimensional discrete particle model for gas-solid fluidized beds on unstructured mesh. *Chem Eng J*. 2009;152:514–529.

40. Hu HH, Joseph DD. Direct simulation of fluid particle motions. *Theoret Comput Fluid Dyn*. 1992;3:285–306.

41. Gidaspow D. Multiphase Flow and Fluidization: Continuum and Kinetic Theory Descriptions. Boston: Academic Press, 1994.

42. Ai J, Chen JF, Rotter JM, Ooi JY. Assessment of rolling resistance models in discrete element simulations. *Powder Technol*. 2011;206: 269-282.

43. Zhou YC, Wright BD, Yang RY, Xu BH, Yu AB. Rolling friction in the dynamic simulation of sandpile formation. *Phys A: Stat Mech Appl*. 1999;269:536–553.

44. Sasic S, Leckner B, Johnsson F. Characterization of fluid dynamics of fluidized beds by analysis of pressure fluctuations. *Prog Energy Combust*. 2007;33:453–496.

45. Doroodchi E, Peng ZB, Sathe M, Abbasi-Shavazi E, Evans GM. Fluidisation and packed bed behaviour in capillary tubes. *Powder Technol*. 2012;223:131–136.

46. Agrawal K, Loezos PN, Syamlal M, Sundaresan S. The role of meso-scale structures in rapid gas-solid flows. *J Fluid Mech*. 2001; 445:151–185.

47. Amritkar A, Deb S, Tafti DK. Efficient parallel CFD-DEM simulations using OpenMP. *J Comput Phys*. 2014;256:501–519.

48. Zhuang YQ, Chen XM, Luo ZH, Xiao J. CFD-DEM modeling of gas-solid flow and catalytic MTO reaction in a fluidized bed reactor. *Comput Chem Eng*. 2014;60:1–16.

49. Yang CZ, Duan YF, Hu HT. Application of CFD-DEM to the study of solid exchange in a dual-leg fluidized bed. *Particuology*. 2013;11: 636–646.

50. Liu DY, Bu CS, Chen XP. Development and test of CFD–DEM model for complex geometry: a coupling algorithm for Fluent and DEM. *Comput Chem Eng*. 2013;58:260–268.

51. Li TW, Garg R, Galvin J, Pannala S. Open-source MFIX-DEM software for gas-solids flows: part II—validation studies. *Powder Technol*. 2012;220:138–150.

52. Li TW, Gopalakrishnan P, Garg R, Shahnam M. CFD–DEM study of effect of bed thickness for bubbling fluidized beds. *Particuology*. 2012;10:532–541.

53. Wang SY, Guo S, Gao JS, Lan XY, Dong Q, Li XQ. Simulation of flow behavior of liquid and particles in a liquid–solid fluidized bed. *Powder Technol*. 2012;224:365–373.

54. Geng YM, Che DF. An extended DEM–CFD model for char combustion in a bubbling fluidized bed combustor of inert sand. *Chem Eng Sci*. 2011;66:207–219.

55. Norouzi HR, Mostoufi N, Mansourpour Z, Sotudeh-Gharebagh R, Chaouki J. Characterization of solids mixing patterns in bubbling fluidized beds. *Chem Eng Res Des*. 2011;89:817–826.

56. Zhou ZY, Pinson D, Zou RP, Yu AB. Discrete particle simulation of gas fluidization of ellipsoidal particles. *Chem Eng Sci*. 2011;66: 6128–6145.

57. Feng YQ, Yu AB. Effect of bed thickness on the segregation behavior of particle mixtures in a gas fluidized bed. *Ind Eng Chem Res*. 2010;49:3459–3468.

58. Li X, Wang SY, Lu HL, Liu GD, Chen JH, Liu YK. Numerical simulation of particle motion in vibrated fluidized beds. *Powder Technol*. 2010;197:25–35.

59. Mansourpour Z, Karimi S, Zarghami R, Mostoufi N, Sotudeh-Gharebagh R. Insights in hydrodynamics of bubbling fluidized beds at elevated pressure by DEM–CFD approach. *Particuology*. 2010;8: 407–414.

60. Wang JW, van der Hoef MA, Kuipers JAM. CFD study of the minimum bubbling velocity of Geldart A particles in gas-fluidized beds. *Chem Eng Sci*. 2010;65:3772–3785.

61. Wu CN, Cheng Y, Ding YL, Jin Y. CFD–DEM simulation of gas–solid reacting flows in fluid catalytic cracking (FCC) process. *Chem Eng Sci*. 2010;65:542–549.

62. Hou QF, Zhou ZY, Yu AB. Computational study of heat transfer in bubbling fluidized beds with geldart a powder. Seventh International Conference on CFD in the Minerals and Process Industries. CSIRO, Melbourne, Australia, December 9–11, 2009.

63. Muller CR, Scott SA, Holland DJ, et al. Validation of a discrete element model using magnetic resonance measurements. *Particuology*. 2009;7:297–306.

64. Malone KF, Xu BH. Particle-scale simulation of heat transfer in liquid-fluidised beds. *Powder Technol*. 2008;184:189–204.

65. Zhang MH, Chu KW, Wei F, Yu AB. A CFD–DEM study of the cluster behavior in riser and downer reactors. *Powder Technol*. 2008; 184:151–165.

66. Tsuji T, Yabumoto K, Tanaka T. Spontaneous structures in three-dimensional bubbling gas-fluidized bed by parallel DEM–CFD coupling simulation. *Powder Technol*. 2008;184:132–140.

67. Di Maio FP, Di Renzo A. DEM-CFD simulations of fluidized beds with application in mixing dynamics. *KONA*. 2007;25:205–216.

68. Zhong WQ, Xiong YQ, Yuan ZL, Zhang MY. DEMsimulation of gas–solid flowbehaviors in spout-fluid bed. *Chem Eng Sci*. 2006;61: 1571–1584.

69. Bokkers GA, van Sint Annaland M, Kuipers JAM. Mixing and segregation in a bidisperse gas–solid fluidised bed: a numerical and experimental study. *Powder Technol*. 2004;140:176–186.

70. Li J, Kuipers JAM. Gas-particle interactions in dense gas-fluidized beds. *Chem Eng Sci*. 2003;58:711–718.

71. Xu BH, Yu AB, Chew SJ, Zulli P. Numerical simulation of the gas–solid flow in a bed with lateral gas blasting. *Powder Technol*. 2000; 109:13–26.

72. Gilabert FA, Roux JN, Castellanos A. Computer simulation of model cohesive powders: influence of assembling procedure and contact laws on low consolidation states. *Phys Rev E*. 2007;75:011303.

73. Zhu HP, Yu AB. The effect of wall and rolling resistance on the couple stress of granuler materials in vertical flow. *Phys A: Stat Mech Appl*. 2003;325:347–360.

74. Khan KM, Bushell G. Comment on "Rolling friction in the dynamic simulation of sandpile formation." *Phys A: Stat Mech Appl*. 2005; 352:522–524.

75. Malone KF, Xu BH. Determination of contact parameters for discrete element method simulations of granular systems. *Particuology*. 2008;6:521–528.

76. Yang RY, Zou RP, Yu AB. Computer simulation of the packing of fine particles. *Phys Rev E*. 2000;62:3900–3908.

77. Wensrich CM, Katterfeld A. Rolling friction as a technique for modelling particle shape in DEM. *Powder Technol*. 2012;217:409–417.

78. Goniva C, Kloss C, Deen NG, Kuipers JAM, Pirker S. Influence of rolling friction on single spout fluidized bed simulation. *Powder Technol*. 2012;10:582–591.
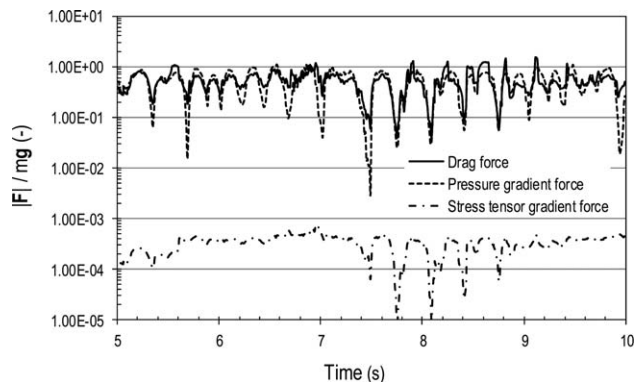
Figure A1. Comparison of the magnitude of different fluid forces normalized by particle gravitational force.

Appendix A: Stress Tensor Gradient Force

When the viscous stress tensor gradient force has been considered, the fluid-particle interaction forces read

$$\mathbf{f}_{f,i} = [-V_i \nabla p + V_i (\nabla \cdot \boldsymbol{\tau}_f)] + \varepsilon \mathbf{f}_{d,i} \quad (A1)$$

where $\boldsymbol{\tau}_f$ is the viscous stress tensor and expressed as

$$\boldsymbol{\tau}_f = \mu_g \left[(\nabla \mathbf{u}_g) + (\nabla \mathbf{u}_g)^{-1} \right] + \left(\lambda - \frac{2}{3} \mu_g \right) (\nabla \cdot \mathbf{u}_g) \overline{\overline{\mathbf{I}}} \quad (A2)$$

Substituting Eqs. A1 and 6 into Eq. 5, the momentum equation of the gas flow becomes

$$\frac{\partial (\varepsilon \rho_g \mathbf{u}_g)}{\partial t} + \nabla \cdot (\varepsilon \rho_g \mathbf{u}_g \mathbf{u}_g) = -\varepsilon \nabla p + \nabla \cdot (\varepsilon \boldsymbol{\tau}_f) + \mathbf{f}'_{sg} + \varepsilon \rho_g \mathbf{g}$$

$$(A3)$$

Simulations considering the viscous stress tensor term in the governing equations were performed under the superficial velocity of 0.9 m/s. The analytical approach was applied for the calculation of local void fraction.

A random particle was selected and tracked through the entire simulation process (i.e., 10 s of gas-solid flow time). Different fluid forces acting on the particle including drag force, PGF, and stress tensor gradient force were monitored and recorded at each time step. The data in the last 5 s were used for analysis. Figure A1 shows the evolution of the magnitudes of drag force, PGF, and viscous stress tensor gradient force (normalized by the particle gravitational force). It can be seen that in comparison to drag and PGFs, the viscous stress tensor gradient force is much smaller (in an order of 10^{-4}). Therefore, the effect of viscous stress tensor term on the simulation results is considered to be negligible and the viscous stress tensor term in the governing equations can be neglected with confidence.

Appendix B: Rolling Resistance Torque

The importance of rolling friction is valid for cohesive particles in gas systems,[72] especially when simulating granular flow with a local voidage close to that of a packed bed (i.e., 0.4), for example, hopper discharge, sand piling, conveying, and packing of granular material.[43,73–76] In above cases, rolling friction plays an important role in stabilizing particles.[72,77]

This study is focusing on free bubbling fluidized beds, in which the average bed voidage is above 0.53. The rolling resistance was, thus, assumed to be negligible, similar to the strategy adopted in the literature.[31,33,35] However, to confirm the validity of the above assumption in the present study, the magnitude of

rolling resistance torque was calculated and compared to the magnitude of the torque generated by the tangential contact force.

The directional constant torque model was used to calculate the resistance torque.[42,43,77,78] The model is expressed as

$$\mathbf{T}_{r,i} = -\sum_{j=0}^{N_{pc}} \mu_r |\mathbf{F}_{n,ij}| \frac{\boldsymbol{\omega}_{ij}}{|\boldsymbol{\omega}_{ij}|} r_i \quad (B1)$$

where μ_r is the rolling friction coefficient depending on the particle material; $\mathbf{F}_{n,ij}$ is the normal contact force; $\boldsymbol{\omega}_{ij}$ is the relative angular velocity between particle i and j as

$$\boldsymbol{\omega}_{ij} = \frac{\boldsymbol{\omega}_i r_i + \boldsymbol{\omega}_j r_j}{r_i + r_j} \quad (B2)$$

As the rolling friction coefficient of the particles used in this study is not available, three values of μ_r, that is, 0.013, 0.065,
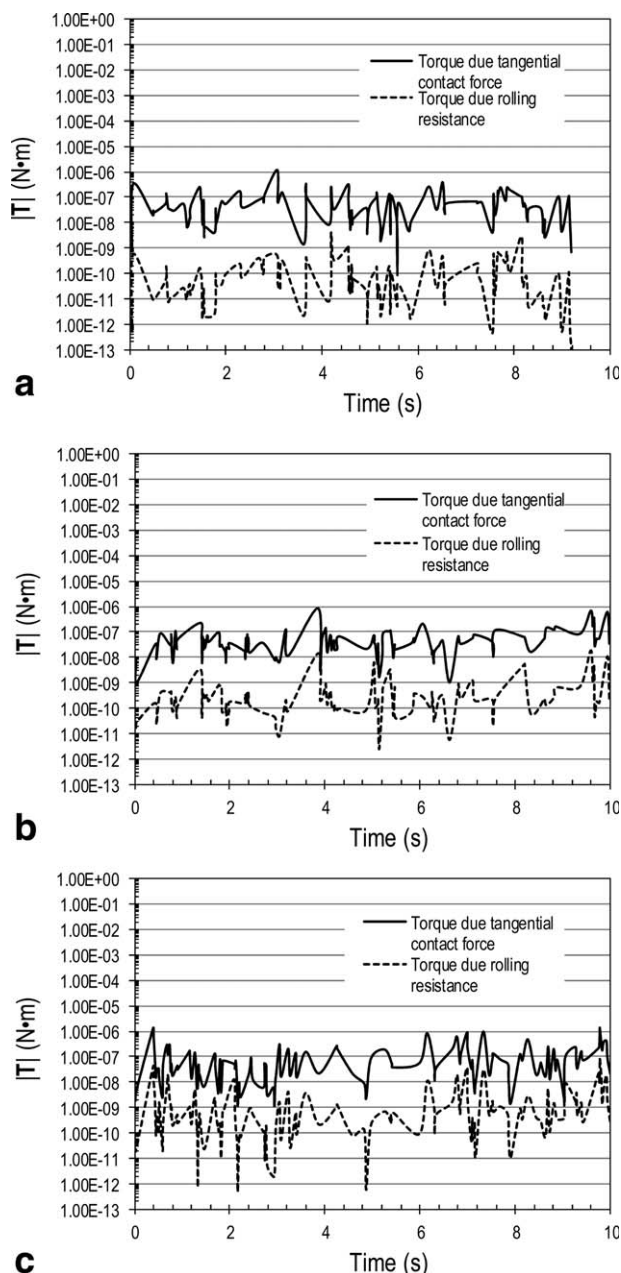
Figure B1. Comparison of the magnitude of torques acting on the particle using a rolling friction coefficient (μ_r) of (a): 0.013; (b) 0.065; (c) 0.13.

and 0.13, were considered. These values cover the range of rolling friction coefficients for typical particle types commonly reported in the literature.[42,43,77,78] The superficial gas velocity was set at 0.9 m/s, as this velocity leads to the densest gas-solid system and gives rise to more particle contacts in comparison to other superficial velocities examined in this study.

The torques (generated by tangential contact force and by rolling resistance) acting on a tracked particle have been monitored and recorded for a simulation time period of 10 s. The time series of the torques are shown in Figure B1. It can be seen that the magnitude of rolling resistance torque is at least 100 times less than the torque due to the tangential contact force. Hence it is reasonable to neglect the rolling resistance torque in the present study.